Bioactive Materials 25 (2023) 160–175

Contents lists available at ScienceDirect

Bioactive Materials

journal homepage: www.keaipublishing.com/en/journals/bioactive-materials

3D bio-printed living nerve-like fibers refine the ecological niche for long-distance spinal cord injury regeneration

Jia Yang [a,1], Kaiyuan Yang [b,1], Weitao Man [b], Jingchuan Zheng [a], Zheng Cao [a], Chun-Yi Yang [a], Kunkoo Kim [a], Shuhui Yang [c], Zhaohui Hou [a], Guihuai Wang [b,**], Xiumei Wang [a,*]

[a] State Key Laboratory of New Ceramics and Fine Processing, Key Laboratory of Advanced Materials, School of Materials Science and Engineering, Tsinghua University, Beijing, 100084, China
[b] Department of Neurosurgery, Beijing Tsinghua Changgung Hospital, School of Clinical Medicine, Tsinghua University, Beijing, 102218, China
[c] School of Materials Science and Engineering, Zhejiang-Mauritius Joint Research Center for Biomaterials, Tissue Engineering Zhejiang Sci-Tech University, Hangzhou, 310018, China

ARTICLE INFO

Keywords:
Neural stem cells
Hydrogels
3D bioprinting
Living constructs
Spinal cord injury

ABSTRACT

3D bioprinting holds great promise toward fabricating biomimetic living constructs in a bottom-up assembly manner. To date, various emergences of living constructs have been bioprinted for *in vitro* applications, while the conspicuous potential serving for *in vivo* implantable therapies in spinal cord injury (SCI) has been relatively overlooked. Herein, living nerve-like fibers are prepared via extrusion-based 3D bioprinting for SCI therapy. The living nerve-like fibers are comprised of neural stem cells (NSCs) embedded within a designed hydrogel that mimics the extracellular matrix (ECM), assembled into a highly spatial ordered architecture, similar to densely arranged bundles of the nerve fibers. The pro-neurogenesis ability of these living nerve-like fibers is tested in a 4 mm-long complete transected SCI rat model. Evidence shows that living nerve-like fibers refine the ecological niche of the defect site by immune modulation, angiogenesis, neurogenesis, neural relay formations, and neural circuit remodeling, leading to outstanding functional reconstruction, revealing an evolution process of this living construct after implantation. This effective strategy, based on biomimetic living constructs, opens a new perspective on SCI therapies.

1. Introduction

Spinal cord injury (SCI) is a ruinous disorder of the central nervous system resulting in permanent motor and sensory dysfunction that imposes substantial somatopsychic suffering and heavy economic burdens on patients. To restore the disrupted neurological functions following SCI, tremendous efforts including surgery, medication, cell therapy, biomaterial implantation, and physical stimulation have been devoted to rebuilding the neural circuits and neuron-based communications post-injury, which however are still far from satisfactory [1]. The dominant reason for the limited therapeutic efficiency is the hostile ecological niche at the damage site that forms gradually accompanying a cascade of pathological events, including inadequate endogenous facilitators, loss of neurons, deteriorating axons and demyelination, ischemia, neuroinflammation, and glial scar formation [2,3]. Hence, refining the ecological niche throughout the injury site has been regarded as a key strategic target in SCI treatment.

Over the past two decades, neural stem cell (NSCs) transplantation has emerged as an encouraging therapeutic option for SCI owing to the dual functions of neurogenic and neuroprotective efforts [4]. It is widely believed that the implanted NSCs with autonomous differentiative capacity can replenish damaged cells, and secrete multitudinous neurotrophic factors acting as a living "biofactory" to nourish the microenvironment, giving rise to the new-born neural circuits and further functional recovery [5]. Moreover, the implanted NSCs could induce the migration of endogenous NSCs into the lesion site to promote spinal cord regeneration [6]. Although NSCs transplantation is considered an aspiring repair strategy, it is commonly faced with an

Peer review under responsibility of KeAi Communications Co., Ltd.
* Corresponding author.
** Corresponding author.
E-mail addresses: guihuai_wang@163.com (G. Wang), wxm@mail.tsinghua.edu.cn (X. Wang).
[1] These authors contributed equally to the work.

https://doi.org/10.1016/j.bioactmat.2023.01.023
Received 5 November 2022; Received in revised form 29 January 2023; Accepted 29 January 2023

inhospitable inflammatory microenvironment resulting in a low retention rate, poor cell survival, uncontrolled migration, differentiation, and high safety concerns, largely reducing the therapeutic effect [4,7,8]. It is noteworthy that the neural stem cells *in vivo* are located in a specific three-dimensional (3D) microenvironment (termed "stem cell niche") comprised of highly active interactions with neighboring cells, the soluble factors, and the extracellular matrix (ECM), which provides structural support for NSC adhesion, and a platform for signal transduction to modulate cell functions such as proliferation, differentiation, migration, and matrix deposition [9]. However, following SCI, the typical structure and function of ECM were severely disrupted. Therefore, biomaterial scaffolds are essential as an artificial ECM to reconstruct the beneficial niches for supporting and modulating cell populations for tissue regeneration. Biomaterial-based stem cell transplantation has gained extensive attention as a promising therapy for SCI that might contribute to the modulation of stem cell functions upon transplantation and avoid the disadvantages of cell therapy [10].

Unlike traditional cell or biomaterial transplantation, the cell-biomaterial construct can form a living biomimetic microtissue to achieve intricate cell-cell crosstalks and cell-materials interactions in a dynamic mode, which might further assemble into tissue- or organ-like architectures at a higher hierarchal level [11]. However, traditional cell seeding or cell encapsulation approaches usually explore "top-down" processing to involve cells in a supporting 3D porous scaffold or hydrogel, often resulting in low seeding density and uncontrolled distribution. Consequently, the bioinspired "bottom-up" strategy has brought a promising prospect for realizing precise assembly of cell-ECM mimetic constructs [12].

3D bioprinting is a revolutionized technology for tissue engineering and regenerative medicine, owing to the excellent ability to build a tissue-like construct in a bottom-up manner by precisely assembling the spatial of cells and hydrogels according to a customized pattern [13–15]. In recent studies, 3D bioprinted NSC-laden microtissues have shown approving validity *in vitro* as developmental and disease modeling and *in vivo* for neural regeneration [16–19]. For example, Mcalpine [20] et al. presented a 3D bioprinted biomimetic scaffold involving neural progenitor cells. It showed an active development into a neuronal network in *vitro*, which revealed the remarkable potential for SCI repair. Zhang [21–23] et al. fabricated a bioprinted scaffold loading NSCs to facilitate functional recovery after SCI by promoting the neuronal differentiation of transplanted NSCs. In addition, encapsulating NSCs into hydrogel could also modulate the degradation properties of the 3D bioprinted scaffolds to match the rates of nerve regeneration [24]. However, although these results pointed out the 3D bioprinted NSC-laden microtissues would be an ideal transplant for SCI therapies, it is still unclear the long-term outcomes of exogenous NSCs *in vivo* and how the living microtissue refines the ecologic niche after SCI, which needs to be further addressed.

Herein, we present a promising strategy for SCI repair. In brief, we fabricated a living microtissue via 3D bioprinting technology using native ECM-like hydrogel carrying a high density of NSCs, which exhibits an oriented spatial arrangement like native nerve fibers. The living fibers were assessed *in vitro*, indicating a conducive NSCs niche for long-term tenable cell viability, permissive cell extension, migration, differentiation into functional neurons, and transmitting signal ability. The pro-regenerative efficacy of these living nerve-like fibers was examined across a 4 mm-long spinal cord complete transection rat SCI model, demonstrating accelerated neural circuits rebuilt and enhanced functional recovery (Fig. 1). With optimizing biological functions and reduced complexity, 3D printed living nerve-like fibers provide new reliable routes for SCI repair, contributing to the follow-up clinical applications.

2. Materials and methods

2.1. Synthesis and characterization of GelMA/HAMA

GelMA was synthesized as described previously with some modifications [25,26]. Briefly, 10 g of type A porcine skin gelatin (Sigma-Aldrich, USA) was fully dissolved with 100 mL Dulbecco's phosphate-buffered saline (DPBS, Invitrogen, USA) at 50 °C, 8 mL methacrylic anhydride (MA, Sigma-Aldrich, USA) was dropwise added to the gelatin solution under vigorous stirring (200 rpm) and reacted for 3 h under 50 °C. The reaction was stopped by adding 5x DPBS to dilute the mixture and dialyzed (12–14 kDa cut-off dialysis membrane) against deionized water at 50 °C for 7 days to remove unreacted MA. The final dialyzed GelMA solutions were lyophilized for 1 week and stored at −80 °C until further use.

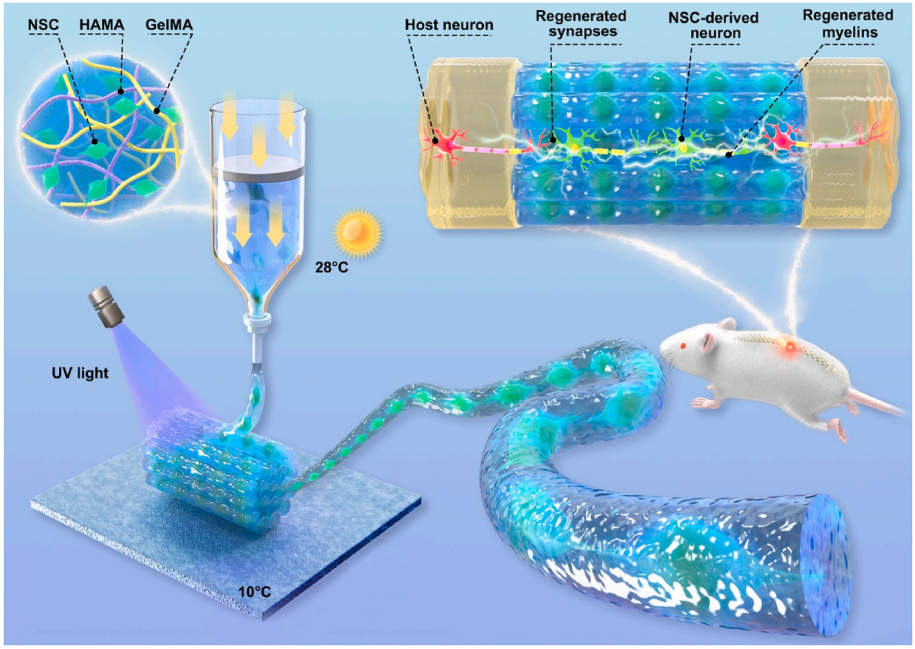

Fig. 1. Scheme showing the fabrication of the 3D bioprinted living nerve-like fibers and the remodeling of the new-born functional network *in vivo*.

HAMA was synthesized according to the previous work [27]. In brief, 1% (v/v) MA was dropwise to a solution of 1 wt% hyaluronic acid (HA, 100–200 kDa, MACKLIN, China) with distilled water and the pH of the mixture was continuously adjusted to 8–9 with 5 M NaOH. The mixture was stirred on ice for 24 h during the reaction, then dialyzed (12–14 kDa cut off dialysis membrane) against deionized water at 4 °C for 3 days to get the purified HAMA solution. Finally, HAMA solutions were lyophilized and stored at −80 °C for further use.

Proton nuclear magnetic resonance (^{1}H-NMR) was used to evaluate the degree of methylation (DM). The Gelatin and GelMA respectively dissolved in deuterium oxide (D_2O, Sigma-Aldrich, USA) at a concentration of 10 mg/mL, as well as HA and HAMA. All the ^{1}H-NMR spectra were obtained at an ambient temperature on a 600 M NMR spectrometer (JNM-ECA600, JEOL Ltd., Japan).

2.2. Hydrogel formation and characterization

The prepolymer solutions were prepared by dissolving 5% GelMA (w/v) and 1% HAMA (w/v) sponge with 0.1% I2959 (w/v) in PBS at 80 °C for 30 min and kept in a 37 °C incubator. The precursor solution (200 μL) was pipetted into a cylindrical poly-tetra-fluoroethylene (PTFE) mold (1 cm^2 S × 2 mm H), followed by 10 mW/cm^2 UV irradiation for 50s achieved by OmniCure S1500 UV lamp (Lumen Dynamics, Ontario, Canada). After curing, the hydrogels were moved from the mold.

The hydrogels were lyophilized and subsequently ground into fine powders, followed by evenly mixing with 100X (w/w) KBr for Fourier transform infrared spectroscopy (FTIR). The spectra of the hydrogels were recorded with wavenumbers ranging from 4000 to 400 cm^{-1} at 1 cm^{-1} resolution and 32 scans per spectrum using the FTIR spectrometer (TG-MS-FTIR-70, NETZSCH Groups, Germany).

The 3D printed scaffolds were treated with lyophilization, followed by sputtering a 10 nm platinum film-coated to the surface before morphology assay using a field emission scanning electron microscopy (SEM, CarlZeiss, Oberkochen, Germany).

A rheometer (MCR301, Anton Paar GmbH, Graz, Austria) equipped with a 25 mm diameter parallel plate was used to measure the rheological properties of the GelMA/HAMA pre-polymers and gelation (Gap size: 600 μm). The temperature dependence of viscosity, storage modulus (G′), and loss modulus (G″) was recorded in the dynamic frequency sweep (1 Hz at 0.1% strain) by increasing temperature from 10 °C to 40 °C at the heating rate of 5 °C/min. The viscosity of the prepolymers was measured using an amplitude sweep at 28 °C as a function of the shear rate from 0.1 to 100 s^{-1}. The UV sensitivity of prepolymers was investigated by oscillatory time sweeps (1 Hz at 0.1% strain) with the measured rate of 8s per point, and UV irradiation with 10 mW/cm^2 was applied to the pre-polymers within 200–250s. Storage (G′) and loss (G″) modulus of the hydrogel were recorded in the dynamic frequency sweep test (0.1–1.02 Hz at 1% strain).

For *in vitro* degradation behavior test, the hydrogel samples (n = 5) were incubated at 37 °C under the conditions: PBS with 0.1 mg/mL collagenase (Sigma, St. Louis, MO, USA), PBS with 0.1 mg/mL hyaluronidase (Sigma, St. Louis, MO, USA), PBS with 0.1 mg/mL collagenase and 0.1 mg/mL hyaluronidase. Followed by monitoring changes in the wet weight of the hydrogels over time.

2.3. Neural stem cells isolation and culture

Neural stem cells (NSCs) were isolated from the dissected hippocampus of E14 embryonic from gestational Sprague-Dawley (SD) rat, as previously described with slight modification [28]. Briefly, the embryonic was separated gently, stripped the endocranium and blood vessels, and extracted the hippocampus in a 10 mm dish with ice-cold Hank's buffered salt solution (Hanks, H1025, Solarbio, China), cut into small pieces, and digested in 0.05% EDTA/Trypsin (Gibco, USA) at 37 °C for 10 min, followed by centrifugation at 200×*g* for 5 min. The cell was cultured in proliferative NSCs medium (Neurobasal™ medium (Gibco, USA) with 2% B27 (Gibco, USA), 1% penicillin-streptomycin (PS, Sigma-Aldrich, St. Louis, MO), 1% glutamax (Gibco, USA), 20 ng/mL basic fibroblast growth factor (bFGF, Solarbio, China), 20 ng/mL epidermal growth factor (EGF, Solarbio, China) in a humidified incubator with 5% CO_2 at 37 °C. The half-volume medium was changed every 2 days, after propagating for about 7–10 days, the NSCs spheres were dissociated with accutase (Invitrogen, USA) into single cells and passaged using a fresh medium. In addition, after 7 days of culture, the NSCs spheres were randomly collected and stained with Nestin (1:100, sc-23927, Santa Cruz, USA) for identification, and images were captured by a confocal laser scanning microscopy (LSM980 Airyscan2, Zeiss, Germany).

Single NSCs were cultured in DMEM/F12 proliferative medium containing 1% N2(Gibco, USA), 2% B27 (Gibco, USA), 1% PS (Sigma-Aldrich, USA), 20 ng/mL bFGF (Solarbio, China), and 20 ng/mL EGF (Solarbio, China) and collected for *in vitro* NSCs viability, morphology, differentiation, and intracellular calcium imaging experiments. For *in vivo* transplantation, the single NSCs were adherent cultured and incubated with DMEM/F12 medium containing lentiviral particles (pLV-EGFP/Puro-CMV, Cyagen Biosciences, China) and polybrene (5 μg/mL) overnight to get GFP-labeled NSCs.

2.4. 3D bioprinting process

All cell-laden scaffold fabrication procedures were achieved in a biosafety cabinet after UV sterilization and 75% ethanol spray. A commercial 3D printing system (Bioscaffold, GeSim, Germany) was employed for the construction of 3D hydrogel scaffolds.

The GelMA/HAMA ink was dissolved in PBS at 50 °C using the same procedure as mentioned above and then added I2959 solution to a final concentration at 0.1% wt%, and afterward stored in an incubator at 37 °C until cell encapsulation. For bioprinting, bioink was obtained by resuspending the NSCs pellet with GelMA/HAMA ink (10^7 cells/mL), and then gently pipetted avoiding air bubbles until homogeneous bioink formation. Ultimately, the NSCs-laden bioink was transferred into a plastic cylinder equipped with a 260-μm nozzle. The temperature of the plastic cylinder loading NSCs-laden bioink was maintained at 28 °C throughout the bioprinting operation. A 12-well plate was placed on the print platform and controlled the temperature at 10 °C, to collect the 3D bioscaffold. Then, the 12-well plate storing 3D bioscaffold was cultivated in an incubator followed by adding of a culture medium. Bioprinting parameters were used as follows: extrusion pressure: 4 kpa; printing speed: 10 mm/s; strand height: 0.15 μm; curing time: 5s per layer; light intensity:10 mW/cm^2; For *in vitro* assay, the bioscaffold was devised as a grid structure (Side length = 10 mm, Height = 2 mm, Stand distance = 1 mm) with adjacent strands arranged in vertical. For *in vivo* study, the model was designed similarly to a cuboid (length = 4 mm, width = 2 mm, height = 2 mm) assembled with layer-by-layer strands (strand distance = 400 μm) arranged in parallel.

2.5. In vitro live/dead staining of encapsulated NSCs

Live/Dead™ staining was performed to evaluate the viability of NSCs encapsulated within the 3D bioscaffold. Shortly, The NSCs-laden 3D bioscaffolds were incubated with Calcein AM (2 μm) at 37 °C for 20 min, followed by washing with PBS three times, incubation with PI (2 μm) at 37 °C for 10 min, and further washing followed. The image was captured by scanning confocal laser microscopy (Zeiss, Airyscan2-LSM980, Germany). Cell Viability was quantitated using ImageJ 1.51 k (Wayne Rasband, NIH, USA) by counting the number of live cells divided by the total cell number, three independent samples were used for statistical analysis.

2.6. In vitro morphology evaluation of encapsulated NSCs

The NSCs-laden 3D bioscaffold was cultured in DMEM/F12 proliferative medium in an incubator containing 5% CO_2 at 37 °C. After culture for 3 days, the NSCs-laden 3D bioscaffold was successively fixed with 4% paraformaldehyde (PFA) for 1 h at 4 °C, permeabilized with 0.3% Triton X-100 (Sigma) diluted in PBS for 10 min, and blocked with 10% normal goat serum (Solarbio, China) dilute in PBS for 1 h. Then the samples were incubated with Rhodamine Phalloidin (RP, Solarbio, China) and DAPI (sc-74421, Santa Cruz, USA) in dark for 40 min. The images were collected with scanning confocal laser microscopy (LSM980 Airyscan2, Zeiss, Germany).

2.7. In vitro neural differentiation of encapsulated NSCs

To investigate the influence of 3D bioscaffold on the differentiation behavior of the encapsulated NSCs, the NSCs-laden 3D bioscaffold was cultured in the differentiation medium (DMEM/F12 medium (Corning, USA), 10% FBS (Gibco, USA), 1% PS) in an incubator containing 5% CO2 at 37 °C for 7 days, respectively, and the culture medium was refreshed every other day. After culturing, the NSCs-laden 3D bioscaffold was fixed in 4% PFA, permeabilized by 0.3% Triton X-100, and blocked with 10% normal goat serum sequentially. Subsequently, the NSCs-laden 3D bioscaffold was incubated with primary antibodies diluted in PBS overnight at 4 °C, washed three times with PBS, followed by incubating with corresponding secondary antibodies and DAPI in dark for 1 h at room temperature. The primary antibodies used were listed as follows: Tuj-1 (1:500, ab18207, Abcam, UK), MAP-2 (1:100, sc-74421, Santa Cruz, USA), GFAP (1:200, ab4648, Abcam, UK). Images were taken with scanning confocal laser microscopy (LSM980 Airyscan2, Zeiss, Germany).

For quantitative real-time polymerase chain reaction (qRT-PCR) assay, the NSCs-laden 3D bioscaffolds were cultured in the proliferative medium or the differential medium for 7 days. Furthermore, the NSCs were cultured on the TCP in the differentiation medium with or without 50 ng/mL nerve growth factor (Solarbio, China) for 7 days, as a positive and negative control, respectively. Total RNA was extracted from the NSCs within the scaffold and TCP by an mRNA kit (Tiangen, China), then reverse transcribed to cDNA using a FastQuant RT kit (Tiangen, China). qRT-PCR was performed with SYBR Green supermix (Bio-Rad, USA) and measured by a CFX96 real-time PCR detection system (Bio-Rad, USA). The primer sequences are provided in Table S1. Target gene expression was normalized by the expression of GAPDH and analyzed using the $2^{-\triangle\triangle Ct}$ method.

2.8. Calcium imaging

According to the manufacturer's experimental protocols, the intracellular Calcium activity in cells was detected using the Fluo-4 Calcium Imaging Kit (Invitrogen, F10489). Briefly, the 3D cell-laden bioscaffold on glass confocal dishes was washed three times using Hanks solution without phenol red, subsequently, fluorescent probes were loaded by incubating Fluo-4 AM solution in Hanks for 30 min at 37 °C, followed by washing 3D cell-laden bioscaffold twice with D-Hanks balanced salt solution (D-Hanks, H1045, Solarbio, China) without phenol red before examined.

Adding 100 μM glutamate (Sigma-Aldrich, USA) diluted in D-Hanks to 3D cell-laden bioscaffold, calcium signals within cells were recorded as videos by scanning confocal laser microscopy (Zeiss, Airyscan2-LSM980, Germany) using confocal Z-stack (10 Slices, Thickness = 18 μm) and time series (7.28 s per frame) imaging. After background correction, the Fluorescence intensity with time series within the region of interest was performed by Zen 2.6 image software (Carl Zeiss, Jena, Germany). The transient booming in fluorescence intensity was regarded as a calcium blinking event.

2.9. Neurons culture and sholl analysis

Primary rat cortical neurons were purchased from Procell (China) and seeded on the NSCs-laden 3D scaffold at a density of 1×10^5 cells per scaffold. After seeding, the samples were cultured in the neuronal adhesion medium (Neurobasal medium, 1% FBS, 2% B27, 1% PS) for 12 h, and then replaced with the neuron maintenance medium (Neurobasal medium, 2% B27, 1% PS) for 1 day before fixing in 4% PFA. Subsequently, the samples were stained with Tuj-1 (1:500, ab18207, Abcam, UK) according to the same procedures described in section 2.7.

Neurons were imaged with scanning confocal laser microscopy (LSM980 Airyscan2, Zeiss, Germany) using a 63× objective. The images were processed by Imaris 9.3.1 3D image visualization software (Bitplane Inc., South Windsor, CT) and analyzed by the "Filament Sholl Analysis" function in Imaris (Sholl Sphere Radius = 3 μm).

2.10. Animal procedures

This study was performed in strict accordance with the recommendations in the Guide for Care and Use of Laboratory Animals of the National Institutes of Health. All Animal procedures were carried out associated in conformity with guidelines evaluated and approved by the Institutional Animal Care and Use Committee of Tsinghua University (Beijing, China, approval number: 18-WXM1), and the laboratory animal facility is fully accredited by Association for Assessment and Accreditation of Laboratory Animal Care International (AAALAC). Health female SD rats (8-week-old, 200–220 g, n = 72) were used in this study. The 4 mm-long complete transection rat SCI models were established under anesthesia with intraperitoneal injection of 1% pentobarbital sodium solution (30 mg/kg). In brief, a midline dorsal skin incision was made, followed by a T8-T10 vertebrae laminectomy. Under the microscope, the dura was opened, and a 4 mm-long T9-T10 spinal cord segment was completely transected and removed by using a combination of microscissors and microaspiration. After transection, the gelfoam was used for hemostasis, preserving the ventral dura mater. The rats were randomly divided into three groups according to different treatments. 3D bioscaffold (scaffold group, S group) or 3D GFP–NSC–laden bioscaffold (NSC-laden scaffold group, SN group) was immediately implanted into the lesion site to fill the cavity. The untreated SCI group without any implants was used as a control (the SCI group, SCI group). Finally, the surgical incisions of muscle and skin were closed with sutures in layers. Following the operation, all rats received Meloxicam (4 mg/kg) for three days and penicillin for seven days. Bladder extrusion was manually applied three times daily until automatic bladder emptying was established.

Biotinylated dextran amine (BDA, Dextran, Alexa Fluor™ 488, 10,000 MW, D1820, Invitrogen, USA) injection was performed at 10-week post-surgery for the tract-tracing of axons (n = 3 for each group). Briefly, the rats were under pentobarbital anesthesia and a second laminectomy procedure was performed to remove the two segments of vertebrae rostral to the injury site. Subsequently, 10% w/v BDA solution was injected into 4 sites (2 sites on each side; 0.5 μL into each site) of the exposed spinal cord using a micropipette (Hamilton, Switzerland) at 0.15 μL per minute [29]. Finally, 2 weeks after BDA injection, these rats were sacrificed, perfused with saline and 4% PFA, obtained the spinal cord tissues, and sliced into 10 μm-thick sections for further tract-tracing evaluation.

2.11. Behavioral assessment

The motor function was assessed weekly after surgery by hind-limb performance, using a locomotor open-field rating scale, the Basso-Beattie-Bresnahan (BBB) scales [30]. The BBB scores were determined by three independent investigators blind to the group assignment. In addition, eight rats of each group were randomly selected at each time point for the BBB test, respectively. An automated CatWalk XT

video-based gait analysis system (Noldus 10.6, Wageningen, The Netherlands) was used to record, evaluate and analyze the footprints of rats. The coordination of voluntary hindlimb movement was evaluated with the inclined-grid climbing test [31], and the grid (15 × 15 mm^2 holes) was at a 45° angle from the horizontal plane. Upon the rats slightly placed at the bottom of the grid, a video was started to record the climbing behavior.

2.12. Electrophysiological assessment

The motor evoked potentials (MEPs) were recorded using an Electromyograph and Evoked Potential Equipment (33A07, Dantec Dynamics, Denmark), as previously described [32]. For the electrophysiological assessment, all rats received the same anesthesia treatment. The bipolar needle electrodes were positioned directly on the skull for the MEP activation. The recording needle electrodes were placed into the tibialis anterior muscle of the bilateral hindlimbs, and a needle electrode was subcutaneously inserted into the back to serve as a ground. The latency (ms) and peak amplitude (mV) of the MEPs were recorded and compared among the groups.

2.13. Histological evaluation

At 1 week and 12 weeks post-surgery, rats were sacrificed for histological evaluation. The rats were deeply anesthetized with pentobarbital sodium and consecutively intracardially perfused with saline and 4% PFA, and the spinal cord segments containing the lesion epicenter were isolated and harvested from each rat. Moreover, the major organs such as the heart, liver, spleen, lung, kidney, and bladder were also collected. Tissue samples were first fixed in 4% PFA at 4 °C overnight, then rinsed in PBS, and placed into 30% sucrose solution at 4 °C for 3 days. Afterward, the tissue specimens were embedded into an optimal cutting temperature compound (OCT, Tissue-Tek OCT Compound, USA) and cut into 10 μm-thick serial sections using a cryostat microtome (CM 1950, Leica, Germany). These tissue sections were stained for standard hematoxylin and eosin (H&E), Masson Trichrome staining, and immunofluorescence. Images of H&E or Masson Trichrome staining were taken with a Pannoramic SCAN scanner (3DHIESTECH, Hungary).

For immunofluorescence staining, the sections were rinsed with PBS, permeabilized with 0.3% Triton X-100 for 2 h, and then blocked with PBS containing 10% normal goat serum for 4 h at room temperature. Then the sections were incubated overnight with mixed primary antibodies (Table S2) at 4 °C, washed with PBS to remove unbound primary antibodies, and incubated with the corresponding secondary antibodies (Table S2) in the dark at room temperature for 1 h. A mounting medium with DAPI (Abcam, UK) was used to stain cell nuclei. Immunofluorescence images were captured with a Zeiss Axio Scan. Z1 scanner (Carl Zeiss, Germany) or scanning confocal laser microscopy (LSM980 Airyscan2, Zeiss, Germany), and processed using Zen 2.6 (Blue edition) software (Carl Zeiss, Germany) under the same parameter. To quantitate the immunofluorescence signal of various groups, representative confocal images were obtained under identical illumination settings and subjected to the consistent procedure, by experimenters from a blind perspective. Afterward, the representative immunofluorescence images were quantitatively analyzed using ImageJ 1.51 k software. Five rats were prepared for each group, three sections were selected for each rat, and three independent areas (250 μm × 250 μm) were extracted randomly from a section as the region of interest (ROI) for further analysis, including both the rostral, center, caudal of the injury site.

After 12 weeks post-surgery, the lesion epicenters in the other 9 rats (3 rats for each group) were harvested, then ultra-thin (60 nm-thick) and semi-thin (500 nm-thick) axial sections were obtained with a microtome (EM UC6, Leica, Germany) [32,33]. The ultra-thin sections were doubly stained with uranyl acetate and lead citrate, then observed with a transmission electron microscope (TEM, Tecnai Spirit, FEI, Czech Republic). The semi-thin sections were stained with toluidine blue solution and images were acquired using a Pannoramic SCAN scanner (3DHIESTECH, Hungary). ImageJ 1.51 k software was used to quantify toluidine blue staining and TEM images.

2.14. Statistical analysis

All data are presented as averages ± standard deviation (SD). One-way factorial analysis of variance (ANOVA) followed by LSD (equal variances) or Dunnett's T3 (unequal variances) post hoc test was utilized to determine statistical differences for multiple comparisons by SPSS (v.26.0; IBM Corp., USA). All tests were conducted two-sided, and values of $^{*}P < 0.05$, $^{**}P < 0.01$, and $^{***}P < 0.001$ were considered statistically significant. Repeated-measures two-way ANOVA was used in the BBB experiment to compare the differences between different groups and time points.

3. Results and discussion

3.1. Bioink design and characterization

Considering the dominant natural ECM components in the central nervous system, we designed a hybrid hydrogel composed of gelatin and hyaluronan to create a specific niche for NSCs-laden 3D bioprinting. The gelatin and hyaluronic acid backbone were chemically functionalized with methacryloyl groups to synthesize GelMA and HAMA with grafting degrees of 60% and 18%, respectively (Figs. S1a–d), which can covalently conjugate together via carbon-carbon double bonds (1640 cm^{-1}) following photopolymerization and form a hybrid network (Fig. S1e). The composite of GelMA (5% w/v) and HAMA (1% w/v) exhibited obvious thermos-responsive behavior around 25–28 °C accompanied by a sharp decrease in viscosity (Fig. S2a) and a sol-gel transition at 28 °C (Fig. S2b). Meanwhile, it showed a typical shear-thinning behavior at 28 °C, which was necessary for protecting cells from shear force damage during the printing process (Fig. S2c). In addition, the GelMA/HAMA solution underwent a fast gelation process under ultraviolet (UV) irradiation (Fig. S2d). Consequently, attributed to the desirable printability of bioink and the optimized 3D printing process, which combined with the thermo-crosslinking and photo-crosslinking, all kinds of customized structures could be easily generated at a high resolution.(Fig. 2a–c, **Video S1**).

Supplementary data related to this article can be found at https://doi.org/10.1016/j.bioactmat.2023.01.023.

The printed 3D scaffold achieved the control of macro-pore and micro-pore size, and exhibited an interconnecting porous structure (Fig. 2d–f) that could effectively facilitate the transport of nutrients and waste products, which is beneficial for the long-term survival of encapsulated cells [34]. Moreover, the 3D printed scaffold could be assembled by a linear alignment of 3D printed fibers, to a dedicated size of the native spinal cord, allowing for the precise adaptation of neural defects (Fig. 2g–h).

Cells respond to the biomechanical properties of the surrounding matrix, which have powerful effects on cell behavior and tissue development [35]. The storage modulus (G′) of the printed hydrogel was approximately 1 kPa (Fig. S3a) that comparable with the native spinal cord matrix, which means biomimetic mechanical property [36]. Moreover, the *in vitro* enzymatic degradation behavior showed that the hybrid hydrogel could be fully degraded either with collagenase or hyaluronidase (Fig. S3b), which is crucial for tissue remodeling *in vivo*.

Overall, the GelMA/HAMA bioink presented great printability and suitable physicochemical properties for NSCs encapsulation and 3D bioprinting.

3.2. 3D bioprinting and characterization of NSC-laden construct in vitro

The NSCs were isolated from the hippocampus of the embryonic SD rats and identified using an anti-Nestin antibody (Fig. S4). To evaluate

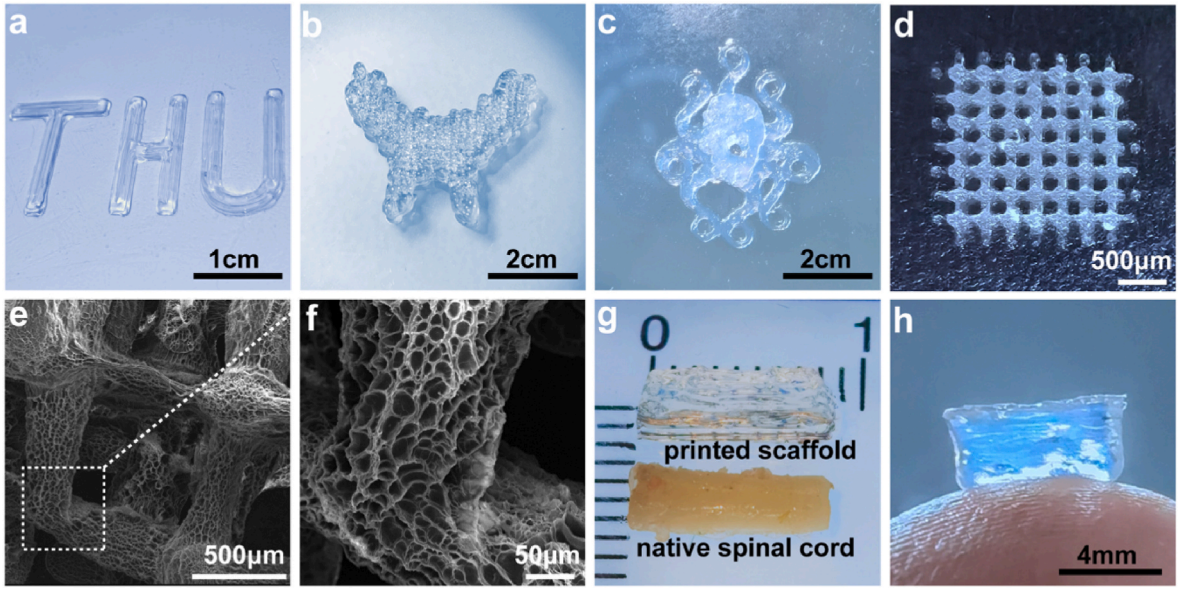

Fig. 2. Fabrication and evaluation of printed scaffolds. a-c) Images of various 3D printed scaffolds. d) Images of 3D printed grid. e-f) SEM images of 3D printed scaffolds. g-h) Photographs of the printed scaffolds assembled with parallel linear arrays.

the cellular viability and functions of NSCs in the GelMA/HAMA following 3D bioprinting, the NSC-laden bioink with a high cell density of 10^7/mL was prepared and printed in a layer-by-layer 3D printing procedure to form a living construct and then transferred into a culture medium and cultured in a humidified incubator. The viability of NSCs inside the construct was evaluated *in vitro* by a Live/Dead staining assay, which showed extremely high viabilities (94.69% ± 2.35%) immediately after printing and could still maintain a high level after 7 days (Fig. 3a and b). To trace the morphology of NSCs encapsulated in the living construct, we conducted cytoskeleton staining after 3-day cell culture (Fig. 3c). It was obvious that NSCs elongated and stretched out filopodia, suggesting that the GelMA/HAMA hydrogel provided a suitable niche for encapsulated NSCs adhesion and spreading. Moreover, the differentiation behavior of the NSCs was monitored by RT-PCR (Fig. S5). The expression of stemness-specific genes Nestin and SRY-box transcription factor 2 (Sox2) of NSCs in the 3D scaffold with the proliferative medium was much higher than the NSCs in other groups, indicating that the 3D scaffold could maintain the self-renewal and pluripotency of NSCs in a serum-free environment. Meanwhile, the notably lower expression of Nestin and Sox2 was detected in NSCs encapsulated by a 3D scaffold in an induced differentiated medium. The NSCs performed significantly higher expression of the neuron-specific genes βIII tubulin (Tuj-1) and much lower expression of the glial fibrillary acidic protein (GFAP) than the NC group. Immunofluorescence

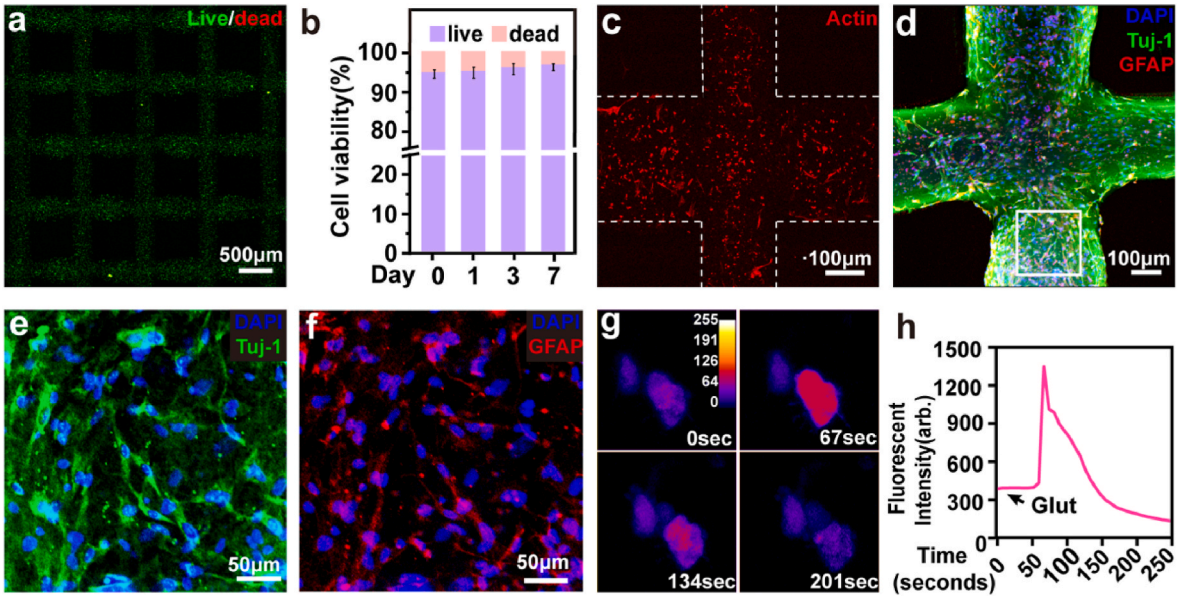

Fig. 3. 3D bioprinting and characterization of NSC-laden scaffolds *in vitro*. a) Live (green)/Dead (red) staining images of 3D bioprinted NSC-laden scaffolds cultured for 0 day. b) Cell viability (%) of 3D bioprinted NSC-laden scaffolds cultured at Day 0 (2 h), Day 1, Day 3, and Day 7. c) Cytoskeleton staining images of 3D bioprinted NSC-laden scaffolds cultured for 3 days. d) Representative images of 3D bioprinted NSC-laden scaffolds cultured for 7 days co-stained DAPI (blue), Tuj-1(green), and GFAP (red). e-f) the enlarged images from the white rectangle of (d). g) Calcium imaging of neurons within 3D bioprinted NSC-laden scaffolds cultured for 14 days. Relative neural activity is shown as color-coded, with signal intensity ranging from black (inactive) to white (high active). Measured and recorded after the addition of the glutamate. h) Time-dependent fluorescent intensity of positive cells shown in (g).

staining was also carried out to visualize the differentiated behavior of the NSCs within the 3D scaffold (Fig. 3d–f), consistent with the PCR result (Fig. S5). It was noticeable that more Tuj-1-positive neurons and relatively fewer GFAP-positive astrocytes were generated within the scaffold. These results indicated that the 3D scaffold endowed the encapsulated NSCs with state-dependent cellular behavior to regulate coordinated sequences of stemness maintenance and neuronal differentiation. Furthermore, intracellular calcium signaling plays a critical role in cellular functions and the signal transduction of all kinds of neurons [37]. To determine whether the neurons that differentiated from NSCs were functional in the 3D living construct, we performed a Flou-4 calcium imaging test 2 weeks after culture. After incubating cells with Flou-4 dye, the fluorescent intensity was monitored by confocal microscopy and recorded in response to neurotransmitters glutamate (Fig. 3g–h). As shown in (**Video S2**), a calcium transient was captured after adding glutamate for 67 s, which indicated that the neurons were functionally active and able to transmit signals by spontaneous activity. As a living construct, the NSCs-laden 3D scaffold is expected to provide a suitable niche for other neurons' adhesion and outgrowth, which may significantly affect integration between host and transplants. Therefore, we investigated the neurite outgrowth of neurons, which seeded on the surface of a 3D printed scaffold for two days. The sholl analysis results suggested that the 3D printed scaffold exerted a positive effect on neurite branches and neuronal maturation (Fig. S6). Collectively, the NSCs-laden 3D bioprinted scaffold exhibited a great function of neurogenesis *in vitro*.

Supplementary data related to this article can be found at https://doi.org/10.1016/j.bioactmat.2023.01.023.

3.3. Regulation of immune microenvironment in vivo

To evaluate the reparative effects of the 3D bio-printed living nerve-like fibers in SCI, we transplanted the living construct to the damaged site (Fig. S7) and kept the SCI rats for 12 weeks (Fig. S8).

Spinal cord injury triggers a battery of inflammatory events in the lesion core, with a peak about 7 days after injury. In this context, the inflammatory microenvironment holds vital importance for the survival of the transplanted NSCs *in vivo* and their long-term nerve repair effect

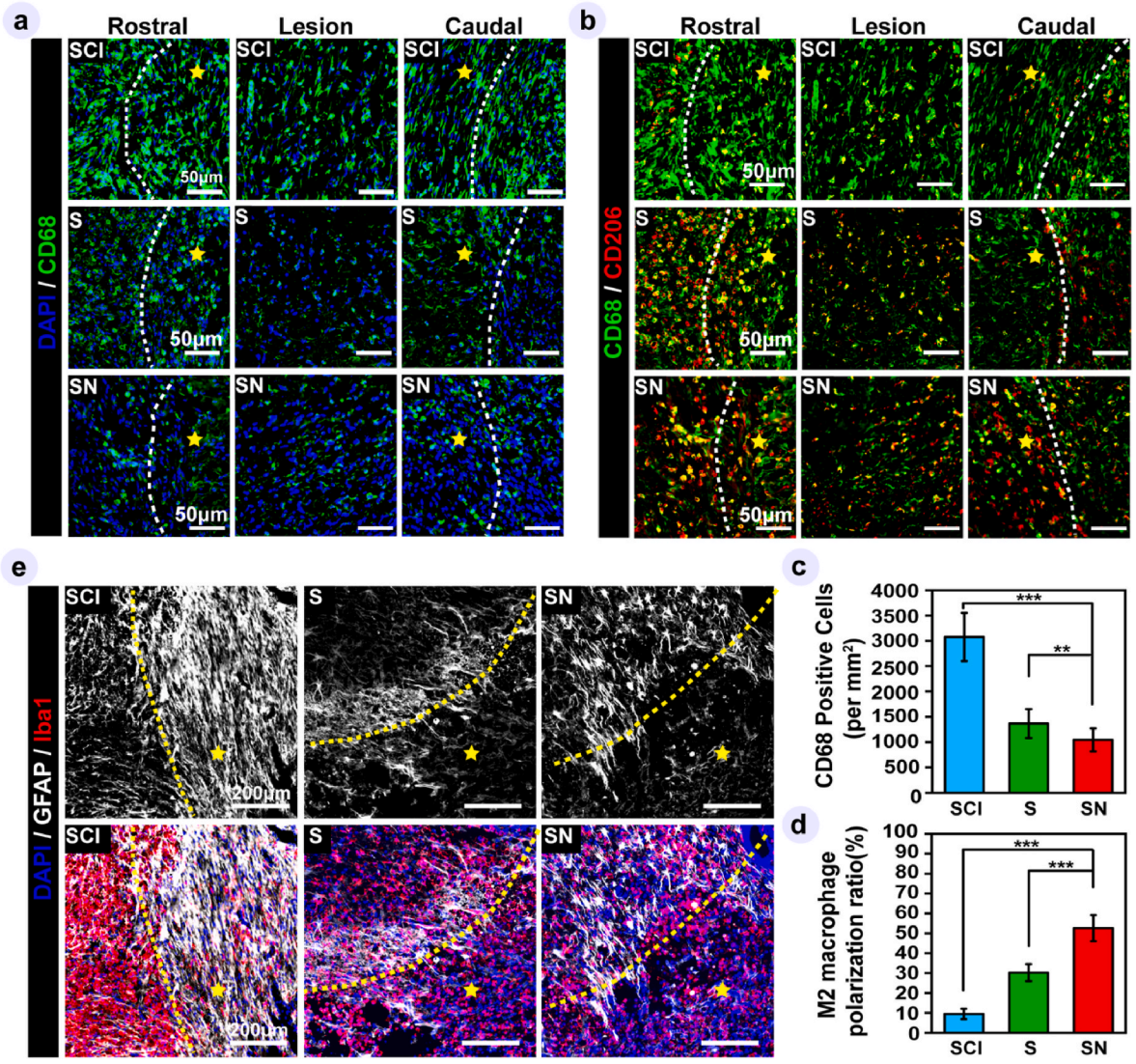

Fig. 4. The living nerve-like fibers regulate the inflammatory response. a-b) Representative CD68 (green), CD206 (red), and DAPI (blue) immunofluorescence staining images of the rostral, lesion, and caudal in the injured spinal cord of three groups, 1 week post-injury. c-d) Quantification of the density of CD68-positive, the polarization ratio of M2 macrophage, respectively. e) Representative images of immunohistochemical staining of the DAPI (blue), GFAP (white), Iba1 (red) in the injured sites of the three groups. All data represented the mean ± SD (n = 5). $^{*}P < 0.05$, $^{**}P < 0.01$, $^{***}P < 0.001$. Dotted lines mark the boundaries between the lesion site and the host spinal cord. the yellow pentagrams indicate the lesion site.

[38].

Microglia/macrophages are critical regulatory cells in the inflammatory process after SCI [39]. Therefore, we performed CD68 immunofluorescence staining to characterize the activation of total macrophages/microglia (Fig. 4a and Fig. S9) and co-labeled it with CD206 to localize the M2-polarized macrophages/microglia (Fig. 4b and Fig. S9). It is well documented that the transition of macrophage phenotypes from pro-inflammatory M1 to anti-inflammatory M2 is of particular importance in guidance tissue repair [40,41]. However, this transition is usually stagnant in SCI.

In our study, we found that the S group exhibited a significantly decreased number of active macrophages ($P < 0.001$) and a significantly increased ratio of M2 macrophages (M2 ratio = 30.91 ± 4.65%, $P < 0.001$) than the SCI group (Fig. 4c–d), indicating a favorable inflammatory regulatory function of implantation with the ECM-like scaffold. These results could be explained by the fact that the implanted scaffold regulated the infiltration and polarization of macrophages due to its mechanical properties [42], porous structure with suitable pore diameters [43,44], and biomimetic ECM components [45,46]. Notably, in comparison to the S group, the number of activated macrophages in the SN group was significantly reduced ($P < 0.01$), and the percentage of M2 macrophages (M2 ratio = 53.83 ± 5.78%, $P < 0.001$) was significantly raised (Fig. 4c–d), suggesting the NSCs within the living nerve-like fibers also showed conspicuous anti-inflammatory function, which might due to the complex interaction between the inflammatory cytokines and the cytokines secreted by NSCs [47,48]. Moreover, a previous study has shown that the nucleic acid drug reprogrammed Schwann cells could facilitate macrophages into M2 phenotype through enhanced intercellular communications, which demonstrated the importance of cell-cell crosstalk in modulate immune signaling [49]. In our study, as a multifunctional system, the living nerve-like fibers could create favorable niche for the encapsulated NSCs to amplify the ability of NSCs to modulate the polarization of infiltrated macrophages. The ECM-like hydrogel and the loaded NSCs acted synergistically, leading to an enhancement cell-cell communication and cell-biomaterial interaction at the post-injury immune microenvironment, which could effectively direct the recruited macrophages into the M2 phenotype and alleviate the local inflammatory response. Collectively, the living nerve-like fibers presented outstanding immunoregulatory function by the synergistic response of hydrogels and NSCs to the inflammatory microenvironment, contributing to accelerating the inflammatory state from pro-inflammation to anti-inflammation, and motiving damaged tissue towards repair and regeneration.

Astrocytes are now considered a highly plastic player following SCI, which could be activated and respond to the inflammatory environment [50,51]. To investigate how the living nerve-like fibers regulate astrocytes during the acute inflammation stage, we labeled the astrocytes and the microglia/macrophages with glial fibrillary acidic protein (GFAP) and Iba-1, respectively (Fig. 4e). Notably, in the SCI group, a large amount of activating astrocytes had migrated to the lesion site and formed a dense wall-like construct, and created a palisade-like border isolating the adjacent host spinal cord and lesion core (Fig. 4e). This wall-like structure formed by intensely activated astrocytes may build a physical and chemical barrier to axon growth [52]. Conversely, loosely arranged astrocytes were found at the lesion edge in a bridge-like pattern for connecting the host spinal cord and implants in the S and SN group (Fig. 4e), indicating that the astrocytes were in a naive state rather than a scar-forming state, owing to the suppression of macrophage activation [53]. Furthermore, this bridge-like astrocyte could serve as a support for the spared axons and guide them to grow across the lesion core, contributing to neural network reconstruction. Meanwhile, hematoxylin-eosin (H&E) staining results also proved that the living nerve-like fibers largely inhibited scar formation caused by the inflammatory storm and created a smooth border for axon growth (Fig. S10).

3.4. Rebuild the niche of the newborn neurons

Chondroitin sulfate proteoglycans (CSPGs), which are mainly secreted by reactive glial scars, have been proven as a dominating inhibitor in axonal plasticity, resulting in the failure of nerve regeneration after SCI [52,54]. We further analyzed the inhibitory effect of CSPGs on axonal growth cones in different groups by staining CS-56 to label CSPGs, and staining GAP43 (Fig. 5a) to label axonal growth cones, at 12 weeks post-injury. In the SCI group, the large number of CSPGs deposited in the damaged site formed a densely chemical barrier, obstructing the host nerves growing across the boundary into the injured area. (Fig. 5a1). Additionally, the enlarged images indicated that regenerating axons stopped at CSPG-rich regions (Fig. 5a4–a5). This is because axonal growth cones are highly sensitive to the characteristics of the microenvironment. Once they reached the lesion core containing abundant CSPGs, they halted and formed dystrophic retraction bulbs [52]. Due to the immunomodulatory effect of the ECM-like hydrogel, the CS-56-positive areas in the S group were obviously decreased, and some budding axons were observed across the injured boundary (Fig. 5a2). Notably, there were few CS-56-positive areas in the SN group that were replaced with a high density of GAP43-positive axons in a relatively aligned pattern instead, which suggested that robust neural axons regeneration was underway in the lesion site (Fig. 5a3).

As the newborn neurons undergo proliferation, axonal extension, and neural network formation, synchronous vascularization is required to meet the increasing demand for the exchange of nutrients and metabolism during the neural tissue regeneration process [55]. Therefore, creating a regenerative neurovascular niche for the injured site is essential for newborn neuron functionalization and tissue regeneration [56]. In order to further understand the synergistic regenerative effects of living nerve-like fibers, newborn neurons and blood vessels were observed by immunostaining staining for Tuj-1 and rat endothelial cell antigen-1 (RECA-1) at l2-weeks post-injury (Fig. 5b). In the SCI group, only a limited number of RECA-1 positive cells can be seen from the rostral to the caudal of the lesion site, especially the epicenter, meanwhile, companies with a few Tuj-1 positive cells (Fig. 5b1–b3). In contrast, more and evenly distributed RECA-1 and Tuj-1 positive cells could be observed within the lesion site in both S and SN groups, indicating that newborn neurons were supported by nutritive structures (Fig. 5b4–b6 and 5b7–b9). Notably, confocal z-stack images of the SN group showed that there were some newborn vascular (Fig. 5c–d, yellow arrows) with lumen-like structures that were uniformly regenerated around newborn neurons of the lesion site, which had laid the groundwork for newborn neurons moving towards functionalization. Taken together, the results suggested that the living nerve-like fibers had optimized the niche of nascent neurons by reducing the generation of inhibitory chemical barriers and rebuilding the vascular system, which contributed to maintaining its sustainable function.

3.5. Nerve regeneration and remyelination

For long-distance SCI repair, the replenishment of neurons in the damaged lesion core is the basis for the reconstruction of neural circuits. To identify and assess the neuronal regenerative capacity of the complete transected spinal cord with different treatments, we immunostained neuronal class III β-tubulin (Tuj-1) to visualize new-born neurons, growth-associated protein-43 (GAP43) to visualize regenerated budding axons, and neurofilaments 200 (NF) to visualize mature nerve fibers (Fig. 6). There were plentiful regenerated Tuj-1-positive cells in the injury site of the SN group, which was of great significant increase compared with that of the S group ($P < 0.01$) and the SCI ($P < 0.001$) group (Fig. 6a1–a3 and Fig. 6b4). These results suggested that extremely limited neurons could regenerate without any treatment. Meanwhile, in the S group, due to the function of immunomodulation of the ECM-like hydrogel, the formation of scar tissues was reduced, therefore it allowed spared neurons migration into the lesion site. While the living nerve-like

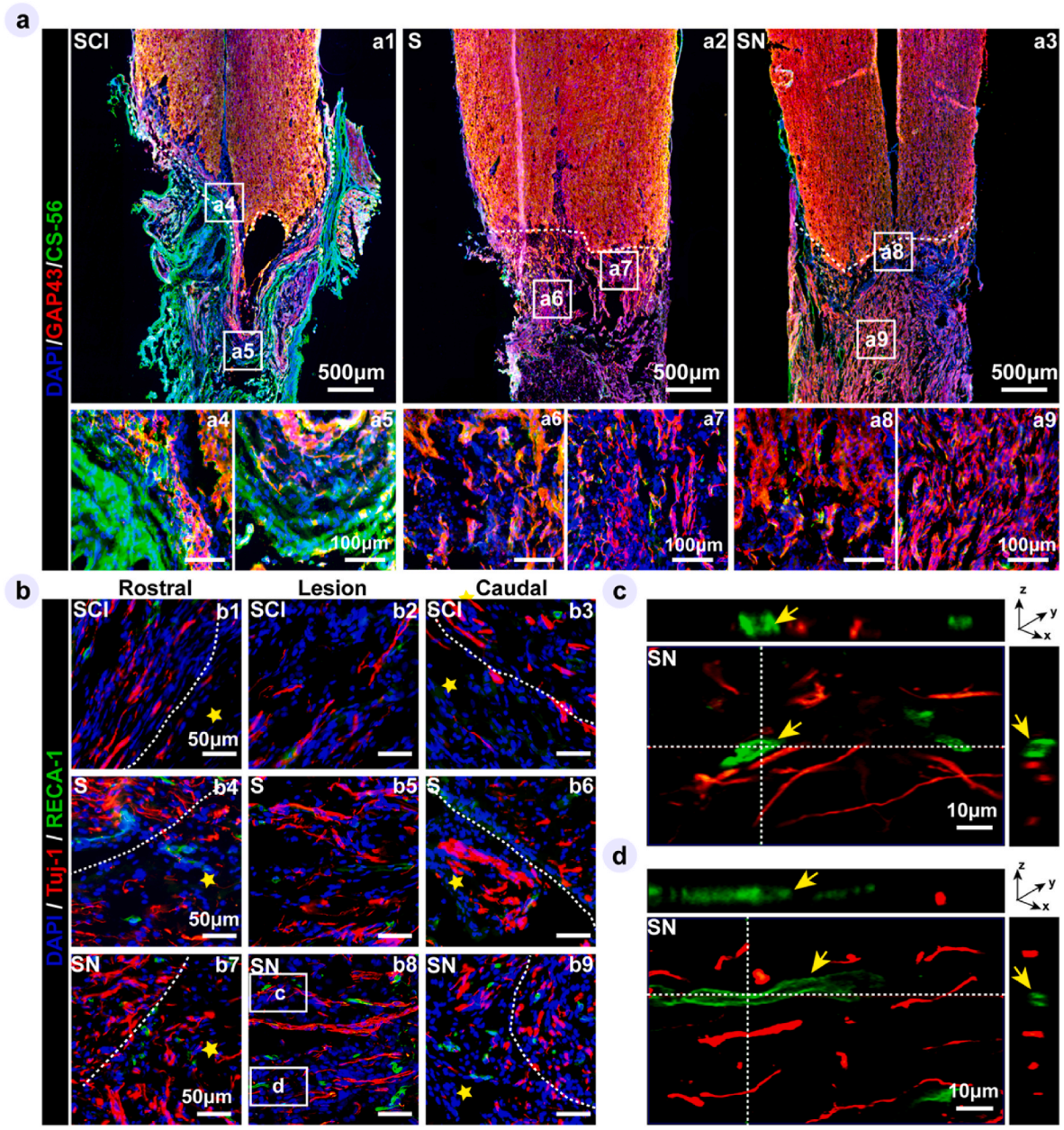

Fig. 5. The living nerve-like fibers create a suitable niche for newborn neurons. a) Representative low and higher magnification immunofluorescence images of DAPI (blue), GAP43 (red), and CS-56 (green), in three groups, 12 weeks post-injury. a4-a9) are enlarged images from (a1-a3). b) Representative DAPI (blue), Tuj-1 (red), and RECA-1(green) immunofluorescence images of the rostral, lesion, and caudal in the injured spinal cord, in three groups, 12 weeks post-injury, the yellow pentagrams indicate the lesion site. Dotted lines mark the boundaries between the lesion site and the host spinal cord. c-d) High-magnification Z-stack images of lesion site in SN group; Arrows, classical blood vessel structure.

fibers not only built a favorable niche for spared neurons but also replenished copious neurons from the neurogenesis of exogenous NSCs in situ. The growing direction of axons is highly sensitive and arborizes their terminals toward correct targets by integrating external cues, suggesting the importance of the guidance of growing direction [57]. Compared with the SCI and S groups (Fig. 6a4 and Fig. 6a5), the GAP43 positive axons in the SN group (Fig. 6a6) were arranged in a relatively uniform and oriented pattern, which was probably attributable to the high density of NSCs evenly distributed in the printed fibers that can serve as a crucial niche to guide the direction of neuronal extension through direct contact or paracrine means [58]. Quantitative analysis of GAP43 positive axons presented that the SN group had the highest density of budding axons compared with SCI ($P < 0.001$) and S group ($P < 0.001$), which demonstrated a desirable niche for regenerating axons provided by the 3D-printed living nerve-like fibers (Fig. 6b8). Most importantly, in contrast with the SCI (Fig. 6a7) and S (Fig. 6a8) groups, abundant nerve fibers had regenerated not only at the lesion edge but also the lesion core and distributed consecutively in the SN group (Fig. 6a9), indicating the homogeneous, rapid, and robust nerve regeneration capacity of living nerve-like fibers. As is shown in Fig. 6b12, quantitative analysis of NF-positive density ($20.75 \pm 3.9\%$) in the SN group was significantly higher than that in the S group ($9.55 \pm 3.27\%$, $P < 0.001$) and the SCI group ($2.62 \pm 1.08\%$, $P < 0.001$), further confirmed the desirable nerve regeneration effect of living nerve-like fibers. Collectively, these results revealed that the living nerve-like fibers 3D assembled by ECM-like hydrogel and ample NSCs provided a superior platform for better nerve regeneration.

Myelin ensheaths axons, electrically insulating the axons and

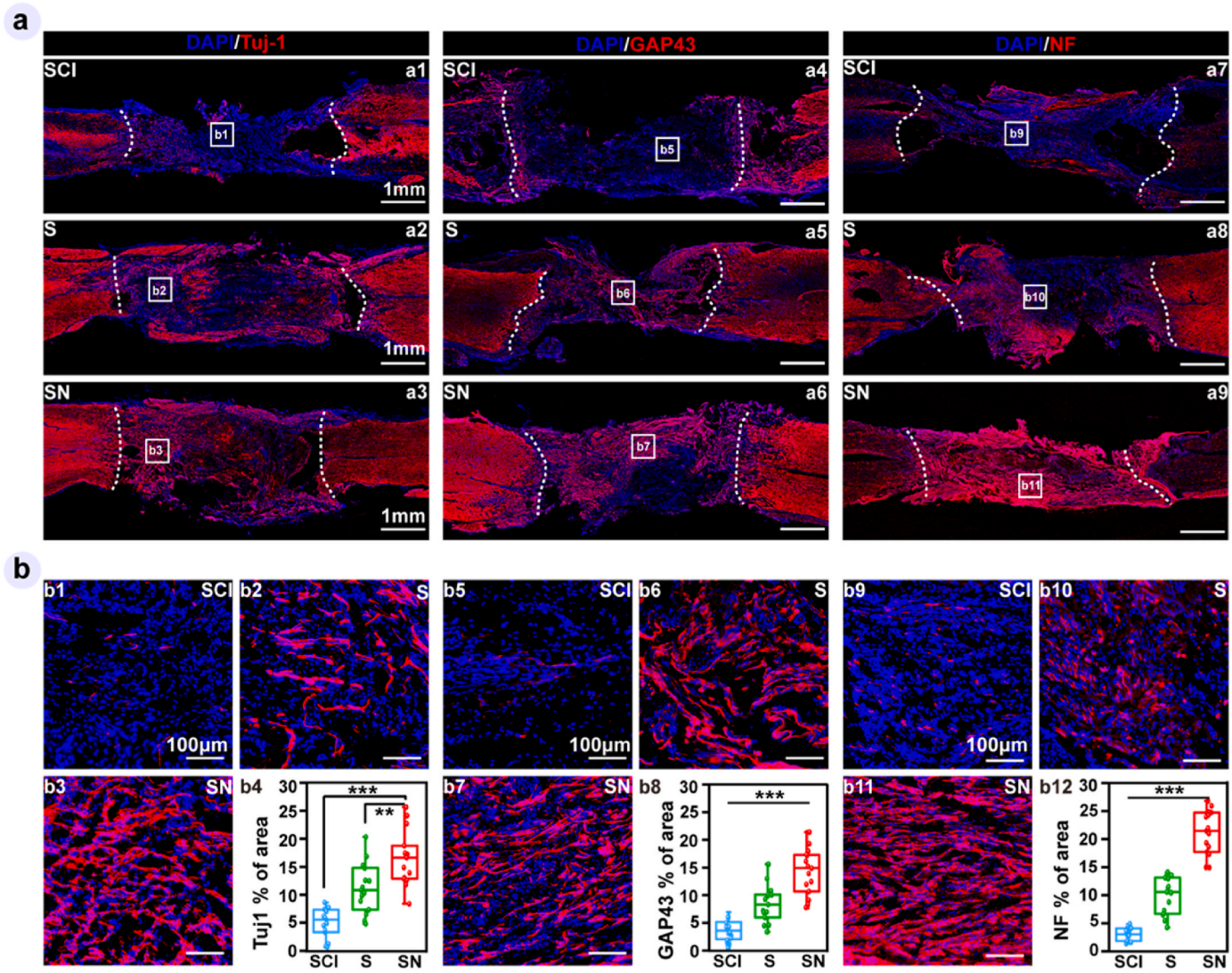

Fig. 6. The living nerve-like fibers enhance nerve regeneration. a1-a3) Representative immunofluorescence images of a longitudinal section in three groups spinal cord co-staining for DAPI (blue) with Tuj-1 (red), 12 weeks post-injury. b1-b3) enlarged images from a1, a2, a3, respectively. a4-a6) Representative immunofluorescence images of a longitudinal section in three groups spinal cord co-staining for DAPI (blue) with GAP43 (red), 12 weeks post-injury. b5-b7) enlarged images from a4, a5, a6, respectively, 12 weeks post-injury. a7-a9) Representative immunofluorescence images of a longitudinal section in three groups spinal cord co-staining for DAPI (blue) with NF (red), 12 weeks post-injury. b9-a11) enlarged images from a7, a8, a9, respectively. b4) Quantitative analysis of Tuj1-positive axons density, b8) GAP43 -positive axons density, and b12) NF-positive axons density, respectively (positive immunoreactive area/total area); A boxplot shows the minimum, first quartile, medium, third quartile, and maximum of the data; $^{*}P < 0.05$, $^{**}P < 0.01$, $^{***}P < 0.001$; n = 5.

increasing the velocity and accuracy of nerve conduction, while providing trophic support and protections to axons, indicating the crucial role of remyelination in rebuilding the neuronal signal transduction system [59]. The semi-thin and ultra-thin sections from the lesion site of harvested nerves in all groups, at 12 weeks post-injury, were examined by toluidine blue staining (Fig. 7a) and transmission electron microscopy (TEM) (Fig. 7b), respectively. A large proportion of regenerated nerve fibers had been wrapped with myelin in the SN groups. In contrast, nerve fibers in the S groups showed a lot of regenerated axons while small and thin myelin sheaths. Moreover, in the SCI groups, there were infrequent regenerated axons and myelin sheaths. Quantitative analysis showed that the density of myelinated nerve fibers in the SN group (20225 ± 2747 nerves/mm^2) was significantly higher than the S group (9092 ± 3228 nerves/mm^2, $P < 0.001$) and the SCI groups (2918 ± 656 nerves/mm^2, $P < 0.001$) (Fig. 7c). To further assess the extent of re-myelination, the area-based G-ratio (axon area/the whole myelinated axon area) was calculated by ultrastructural analysis using TEM and presented by a boxplot (Fig. 7d), and a scatter plot (Fig. 7e). In the SN groups, the area-based G-ratio (0.42 ± 0.06) was significantly lower than the S groups (0.53 ± 0.04, $P < 0.001$) and SCI (0.61 ± 0.44, $P < 0.001$) groups, indicating a relatively mature myelin regeneration. Additionally, the G-ratio scatter plot performed that regenerated nerve fibers of the SN groups showed greater myelinated either in small or larger nerve fibers, compared to the S and SCI groups, reflecting a persistent pro-myelinating ability of the living nerve fibers. We then observed the myelination of axons by IF staining longitudinal and transverse sections in the lesion site using myelin basis protein (MBP, indicates myelin sheath) and NF (indicates nerve fiber), respectively (Fig. 7f and Fig. S11). In the SN group, the Z-stack co-localization images of the longitudinal sections exhibited the regenerated nerve fibers sheathed with densely and organized myelin (Fig. 7g), and the z sections showed a typical “shell-core” structure comprised of myelin encircling nerve fibers (Fig. 7g). In comparison, such structures were much less prevalent in the S group, and sporadically appeared in the SCI group (Fig. S11). These results suggested that the transplantation of the scaffold could enhance the regrowth of axons, but the regenerated axons

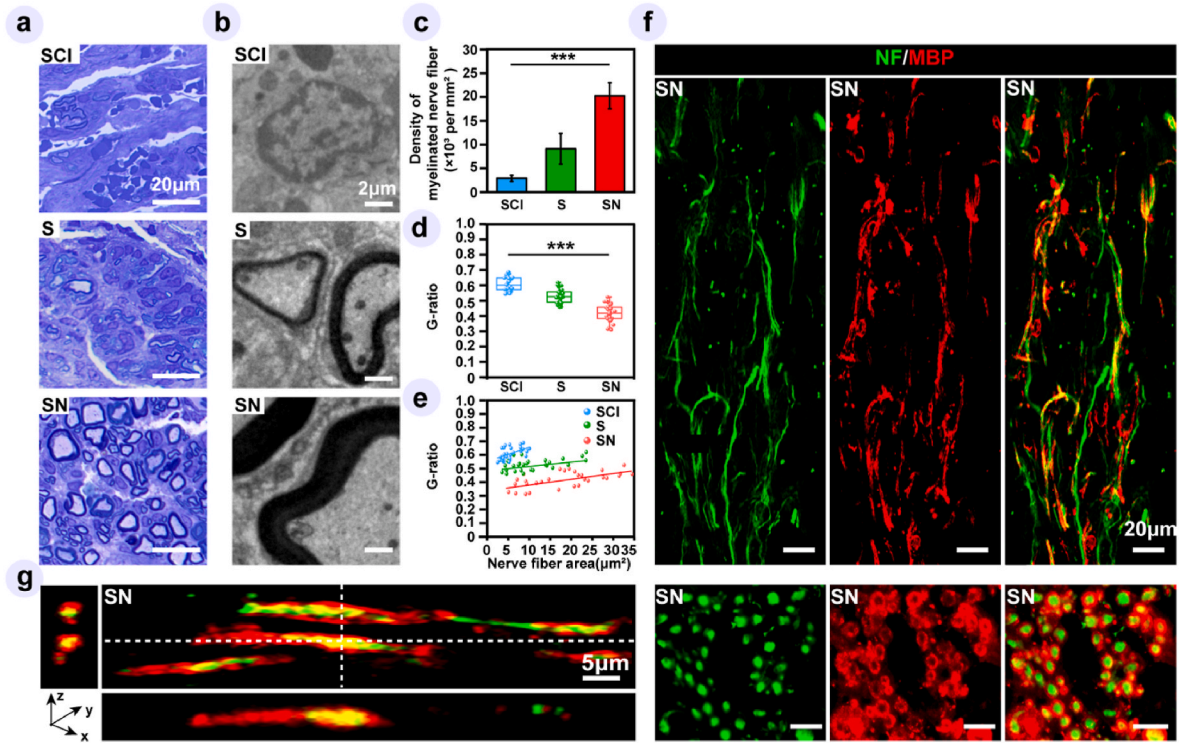

Fig. 7. The living nerve-like fibers facilitate myelin regeneration. a-b) Toluidine blue-stained and TEM images of transverse sections at the lesion site of the SCI, S, and SN groups, respectively. c) Quantitative analysis of the density of the myelinated nerve fiber from toluidine blue-stained images (number/total area). d) Quantitative analysis of the area-based G-ratio from TEM images. A boxplot shows the minimum, first quartile, medium, third quartile, and maximum of the data; e) The scatter diagram of G-ratio versus nerve fiber area from TEM images; $^{*}P < 0.05$, $^{**}P < 0.01$, $^{***}P < 0.001$; n = 3. f) Representative immunofluorescence images of a longitudinal and transverse section in the SN group spinal cord co-staining for NF (green) and MBP (red). g) High-magnification Z-stack images of the lesion site from a longitudinal section in the SN group.

were insufficient, and the reconstruction of myelin was deficient. Meanwhile, the transplantation of living nerve-like fibers to the injury site significantly promoted axon regeneration and remyelination.

3.6. Neural relay formation and functional neural network remodeling

Exogenous NSCs-derived neurons can serve as a "signal relay station" between the host spinal cord and lesion site by forming synaptic connections, which is considered to be a promising and efficient strategy for severe SCI repair [60]. Twelve weeks post-injury, we labeled longitudinal frozen sections of the damaged spinal cord with NF and SYN (Synaptophysin I, a presynaptic marker), thereby visualizing synapse formation between regenerated nerve fibers (Fig. S12). Additionally, in the SN groups, GFP was applied to distinguish between transplanted cells and the host cells (Fig. 8a). The IF staining results showed that transplanted living nerve-like fibers to the injury site achieved extensive and robust neural fibers regeneration throughout the lesion site (Fig. 8a1), in sharp contrast to the S and SCI groups (Fig. S12). Meanwhile, there were many ordered GFP/NF co-positive (indicated grafted-derived neurons) and some NF-positive nerve fibers (indicated the host neurons) at the lesion core in the SN groups. These fibers were densely contacted and had been detected with high-density SYN signals (Fig. 8a2-a6), indicating the new-born synapse formation among the axons from the graft-derived and host neurons. The ultrastructure of regenerated synapses in the SN group was shown by TEM (Fig. 8b). Moreover, quantitative analysis of the percentage of regenerated synapses formed in new-born axons (Fig. 8c) revealed a significant difference ($P < 0.001$) between the N (3.40 ± 1.36%) and SN (10.79 ± 3.62%) groups, reflecting the regenerated neurons in the SN groups possessed an improving connectivity. Overall, these results suggested that the living nerve-like fibers could establish exogenous neuronal relays in the lesion site and integrate with the host neurons, contributing to delivering signals from supraspinal descending pathways.

To explore the functionality of the new-born neuronal network, we identified the regeneration of cholinergic, dopaminergic, and serotonergic axons by staining choline acetyltransferase (ChAT), tyrosine hydroxylase (TH), and 5-hydroxytryptamine (5-HT), respectively. In the SN group, the results displayed a lot of visible NF and ChAT double-stained axons in the lesion site and mostly co-expressed GFP (Fig. 8d1–d3). Similarly, consecutive and abundant NF-positive axons at the lesion site exhibited positive TH and GFP signals (Fig. 8d4-d6). Moreover, the Z-stacks images showed that a 5-HT-positive axon differentiated from grafts exhibited approximately 260 μm extension in the lesion core (Fig. 8d7). In contrast, the staining of functional neurons were rarely observed at the lesion site in other groups (Fig. S13). These findings above demonstrated that the NSCs within the living nerve-like fibers could differentiate into functional neurons associated with movement and sensation. In addition, there were also some non-GFP-expressing functional neurons (i.e., host cells) observed at the lesion site in the SN group, likely due to the improved microenvironment provided by the grafted living nerve-like fibers, leading to the recruitment of some endogenous functional neurons.

We further investigated the reconstruction of descending propriospinal neurons by BDA anterograde tracing (Fig. 8e and Fig. S14), which are involved in interlimb coordination, motor, and sensory recovery after SCI [29]. In the SN group, we discovered abundant BDA-positive neurons in the rostral (Fig. 8e2), lesion (Fig. 8e3), and caudal (Fig. 8e3) of the host spinal cord. However, in other groups, such positive signals were greatly attenuated (Fig. S14). These results demonstrated that the descending propriospinal neurons had regenerated and presented longitudinal axonal projections successfully across the lesion site in the SN group, which validated the reconstruction of the

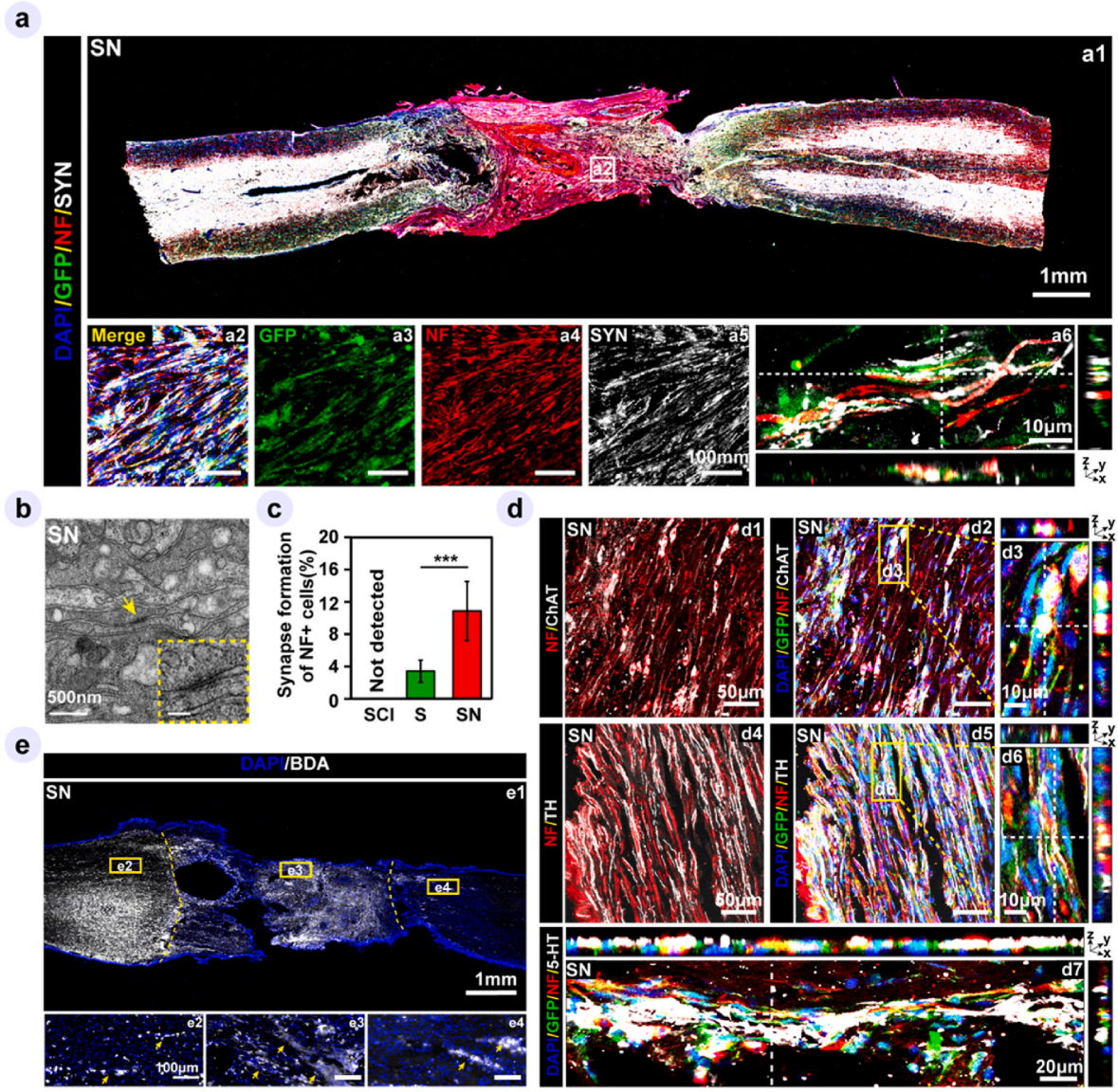

Fig. 8. The living nerve-like fibers remodel a functional neuronal network. a) Representative immunofluorescence images of a longitudinal section in the SN group spinal cord co-staining for DAPI (blue) with GFP (green), NF (red), SYN (white); a2-a5) Enlarged images from (a1); a6) High-magnification Z-stack images staining GFP (green), NF (red), SYN (white) of the SN group. b) TEM images detect the synapse formation in the SN group; the yellow arrow indicates the classical synaptic structure; the yellow dotted rectangle marks the insert, which shows the enlarged images of the synaptic structure. c) Quantitative analysis of the synapse formation ratio within the NF-positive cells. $^{*}P < 0.05$, $^{**}P < 0.01$, $^{***}P < 0.001$; n = 5. d1-d3) Representative images of DAPI (blue), GFP (green), NF (red), and ChAT (white) immunolabeling at the lesion site in the SN group. d4-d6) Representative images of DAPI (blue), GFP (green), NF (red), and TH (white) immunolabeling at the lesion site in the SN group, d7) Representative images of DAPI (blue), GFP (green), NF (red), and 5-HT (white) immunolabeling at the lesion site in the SN group. e) BDA-immunostained sagittal section overview in the SN group. e2-e4) Enlarged images of the rostral, lesion, and caudal in (e1), respectively. Dotted lines mark the boundaries between the lesion site and the host spinal cord.

descending conduction circuits provided by the living nerve-like fibers transplantation.

In summary, the living nerve-like fibers rebuilt a functional network at the lesion site, which was the necessary condition for functional recovery.

3.7. Functional recovery and safety assessment

Following SCI, we used the Basso, Beattie, and Bresnahan (BBB) score weekly to assess the locomotor recovery of rats in the different groups (Fig. 9a). The rats in the SN group demonstrated a statistically significant progressive motor recovery compared with those in the control groups (the N group and the SCI group). Additionally, for the SN group, the rats had recovered from complete paralysis of the hindlimbs after surgery (0 week) to, on average, occasionally weight-bearing dorsal stepping at 12 weeks post-injury (the median BBB score = 9). We further evaluated the voluntary and coordinated motor functional recovery at 12 weeks post-injury using Catwalk analysis (Fig. 9b) and the inclined grid test (Fig. 9c, **Video S3**). The SCI group rats' footprints showed a line-like pattern that indicated persistent dragging of the hindlimbs (Fig. 9b), consistent with the grid test results (Fig. 9c, Video S3), collectively demonstrating negative recovery for motor function. However, the rats in the S group could intermittently lift hindlimbs off the ground (Fig. 9b), and present moderately voluntary movement of hindlimbs while rarely weight-bearing when climbing on the grid (Fig. 9c, Video S3). Notably, in comparison, the rats in the SN group exhibited more obviously intermittent footprints (Fig. 9b) in Catwalk analysis, meanwhile appeared frequent plantar stepping with weight-

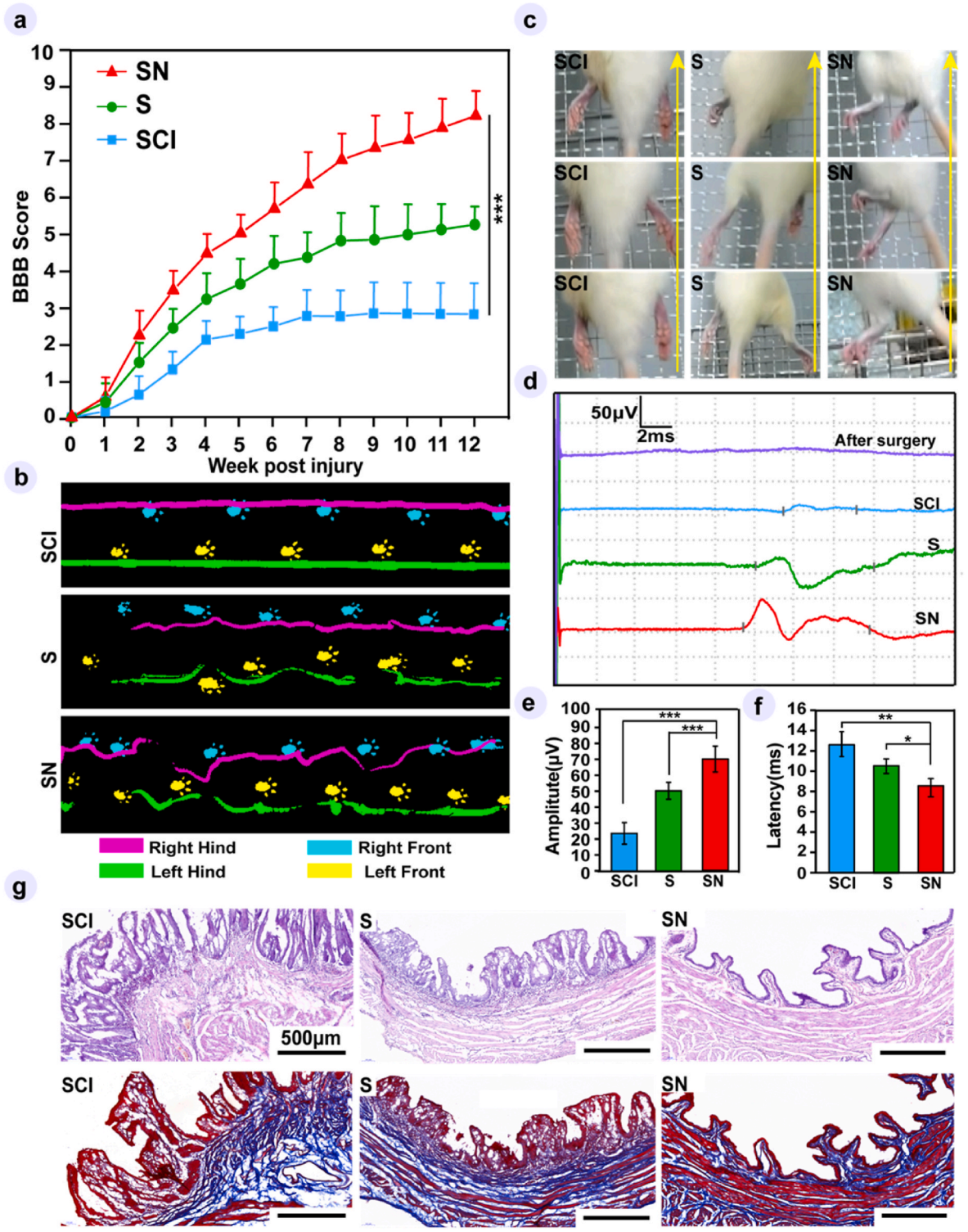

Fig. 9. The living nerve-like fibers promote functional recovery. a) Locomotion-BBB hindlimb scores each week post-injury. Two-way repeated measures analysis of variance (ANOVA). $^{*}P < 0.05$, $^{**}P < 0.01$, $^{***}P < 0.001$; n = 8. b) The representative footprints recorded by the Catwalk system. c) Time series images of the rats' hindlimbs while climbing upward from the bottom; Upward-pointing arrows indicate the direction of time sequences. d) Representative recorded cortical motor evoked potentials (MEP). e-f) Quantitative analysis of MEP amplitude and latency; $^{*}P < 0.05$, $^{**}P < 0.01$, $^{***}P < 0.001$; n = 3. g) H&E staining and mason dyeing images of the bladder tissues.

bearing and occasional forelimb-hindlimb coordination on the inclined grid during climbing (Fig. 9c, Video S3). Furthermore, transcranial electrophysiological tests were performed to excite MEP, the reliable indicator for the capacity of the locomotor signal conduction, in rats of three different groups (Fig. 9d). The results showed a significantly increased MEP amplitude while shortened MEP latency following the order of rats in SCI, S, and SN groups (Fig. 9e–f), indicating that in the SN group, the regenerated neural relay at the lesion site effectively facilitated the conduction of the electrical signals. Collectively, these results provided evidence that the living nerve-like fibers transplantation

enabled an amazing motor functional recovery after SCI.

Supplementary data related to this article can be found at https://doi.org/10.1016/j.bioactmat.2023.01.023.

Urinary system dysfunction constitutes a familiar yet severe complication of SCI and results in a life-threatening consequence [61]. To further investigate the urinary system changes after SCI in different treatments, we examined the pathological characteristics in rats' bladders (Fig. 9g) and kidneys (Fig. S15) in three groups, 12 weeks post-injury. The results indicated that transplantation of living nerve-like fibers could prevent the pathological damage of the bladder in SCI rats from the edema of the mucous membrane and the muscle bundle disorder; This contribution was due to its remarkable anti-inflammatory effect exerted not only in the local spinal cord but the whole body. Studies on kidney tissue reflected similar results (Fig. S15). These findings suggested that SCI rats treated with the living nerve-like fibers, while promoting neurological regeneration, also protected the rats from severe urinary complications.

Additionally, there were no noticeable pathological differences in the hearts, livers, spleens, and lungs performed by H&E staining in all groups (Fig. S16), indicating reliable biosafety of the living nerve-like fibers.

Overall, the 3D bio-printed living nerve-like fibers represent a promising strategy for maximizing the therapeutic potential of NSCs for SCI repair. Our results provided evidence that the ECM-like hydrogel protected exogenous NSCs from the harsh inflammatory environment and supplied a hospitable niche for the NSCs' long-term survival, neural lineage differentiation, and functional synapse formation. Moreover, the ECM-like hydrogel could home the exogenous NSCs in situ due to the support and adhesion effect, while guiding endogenous neuron migration by structural clues to the lesion site. In this way, the exogenous NSCs-derived regenerated neural circuits were recognized, admitted, and integrated by the host spinal cord, which suggested that the 3D printed living constructs *in vivo* matured into truly living tissue, achieving the replacement of lost tissue. Owing to the biomimetic structure and component of the 3D bio-printed living nerve-like fibers, the ECM-like hydrogel synergistic with the carried exogenous NSCs exert an outstanding ecological niche rebuilding function, orchestrates the efficient immunoregulation, neurogenesis, vascularization, remyelination, neural relays formation, and neural circuits remolding, which worked together and remarkably expedited long-distance SCI repair and motor functional recovery.

4. Conclusion

In summary, living 3D nerve-like fibers composed of pluripotent NSCs and ECM-mimic hydrogel was assembled in a bottom-up way achieved by 3D bioprinting technology. The highly homogenous and continuous pro-neurogenesis property of the living nerve-like fibers is vital for long-distance SCI repair. The 3D ECM-mimic hydrogel provided a homeostatic niche for a large amount of NSCs distributed uniformly within the 3D printed nerve-like fibers, allowing encapsulated NSCs to maintain high viability and active intercellular communications. The implantation of the living nerve-like fibers can modulate the microenvironment, promote neurogenesis, neural relays formation, neural circuits remolding, and bridge the spinal cord stumps guiding integration between the renascent network and remaining host tissue, resulting in efficient functional recovery. Taken together, we used 3D bioprinting techniques to build a living 3D construct with optimized function and reduced complexity for SCI repair. Considering the complexity of the SCI microenvironment, designing specifically functionalized artificial spinal cord-like biomaterials to exert synergistic multimodal cues, which could precisely regulate multiple aspects of stem cell behavior and reconstruct the niche more efficiently, may become the next frontier in biomaterials application for spinal cord tissue regeneration in the future.

Declaration of competing interestDoCI

The authors declare that they have no known competing financial interests or personal relationships that could have appeared to influence the work reported in this paper.

CRediT authorship contribution statement

Jia Yang: Conceptualization, Methodology, Investigation, Validation, Formal analysis, Writing – original draft, Writing – review & editing. **Kaiyuan Yang:** Methodology, Investigation, Formal analysis, Writing – original draft, Writing – review & editing. **Weitao Man:** Methodology, Investigation, Resources, Funding acquisition. **Jingchuan Zheng:** Methodology, Validation, Formal analysis. **Zheng Cao:** Methodology, Investigation, Validation. **Chun-Yi Yang:** Methodology, Investigation, Resources. **Kunkoo Kim:** Investigation, Validation, Formal analysis. **Shuhui Yang:** Methodology, Investigation, Formal analysis. **Zhaohui Hou:** Investigation, Validation. **Guihuai Wang:** Supervision, Methodology, Investigation, Validation, Resources, Project administration, Funding acquisition. **Xiumei Wang:** Supervision, Conceptualization, Methodology, Investigation, Validation, Formal analysis, Resources, Project administration, Funding acquisition, Writing – review & editing.

Acknowledgements

The authors thank the financial support from the National Natural Science Foundation of China (Grant No. 32271414 and 82201521), the Tsinghua Precision Medicine Foundation (Grant No. 2022TS001), and the National Key Research and Development Program of China (Grant No.2020YFC1107600).

Appendix A. Supplementary data

Supplementary data to this article can be found online at https://doi.org/10.1016/j.bioactmat.2023.01.023.

References

[1] S.G. Varadarajan, J.L. Hunyara, N.R. Hamilton, A.L. Kolodkin, A.D. Huberman, Central nervous system regeneration, Cell 185 (1) (2022) 77–94, https://doi.org/10.1016/j.cell.2021.10.029.
[2] M.V. Sofroniew, Dissecting spinal cord regeneration, Nature 557 (7705) (2018) 343–350, https://doi.org/10.1038/s41586-018-0068-4.
[3] B. Fan, Z. Wei, X. Yao, G. Shi, X. Cheng, X. Zhou, H. Zhou, G. Ning, X. Kong, S. Feng, Microenvironment imbalance of spinal cord injury, Cell Transplant. 27 (6) (2018) 853–866, https://doi.org/10.1177/0963689718755778.
[4] P. Assinck, G.J. Duncan, B.J. Hilton, J.R. Plemel, W. Tetzlaff, Cell transplantation therapy for spinal cord injury, Nat. Neurosci. 20 (5) (2017) 637–647, https://doi.org/10.1038/nn.4541.
[5] I. Fischer, J.N. Dulin, M.A. Lane, Transplanting neural progenitor cells to restore connectivity after spinal cord injury, Nat. Rev. Neurosci. 21 (7) (2020) 366–383, https://doi.org/10.1038/s41583-020-0314-2.
[6] B. Gong, X. Zhang, A.A. Zahrani, W. Gao, G. Ma, L. Zhang, J. Xue, Neural tissue engineering: from bioactive scaffolds and in situ monitoring to regeneration, Explorations 2 (3) (2022), https://doi.org/10.1002/exp.20210035.
[7] R. Matta, A.L. Gonzalez, Engineered biomimetic neural stem cell niche, Curr. Stem. Cell Rep. 5 (3) (2019) 109–114, https://doi.org/10.1007/s40778-019-00161-2.
[8] B. Yang, C. Liang, D. Chen, F. Cheng, Y. Zhang, S. Wang, J. Shu, X. Huang, J. Wang, K. Xia, L. Ying, K. Shi, C. Wang, X. Wang, F. Li, Q. Zhao, Q. Chen, A conductive supramolecular hydrogel creates ideal endogenous niches to promote spinal cord injury repair, Bioact. Mater. 15 (2022) 103–119, https://doi.org/10.1016/j.bioactmat.2021.11.032.
[9] A. Ranga, S. Gobaa, Y. Okawa, K. Mosiewicz, A. Negro, M.P. Lutolf, 3D niche microarrays for systems-level analyses of cell fate, Nat. Commun. 5 (2014) 4324, https://doi.org/10.1038/ncomms5324.
[10] H. Shen, C. Fan, Z. You, Z. Xiao, Y. Zhao, J. Dai, Advances in biomaterial-based spinal cord injury repair, Adv. Funct. Mater. 32 (13) (2022), 2110628.
[11] T. Kamperman, M. Karperien, S. Le Gac, J. Leijten, Single-cell microgels: technology, challenges, and applications, Trends Biotechnol. 36 (8) (2018) 850–865, https://doi.org/10.1016/j.tibtech.2018.03.001.
[12] V.M. Gaspar, P. Lavrador, J. Borges, M.B. Oliveira, J.F. Mano, Advanced bottom-up engineering of living architectures, Adv. Mater. 32 (6) (2020), e1903975, https://doi.org/10.1002/adma.201903975.

[13] A.C. Fonseca, F.P.W. Melchels, M.J.S. Ferreira, S.R. Moxon, G. Potjewyd, T. R. Dargaville, S.J. Kimber, M. Domingos, Emulating human tissues and organs: a bioprinting perspective toward personalized medicine, Chem. Rev. 120 (19) (2020) 11128–11174, https://doi.org/10.1021/acs.chemrev.0c00342.
[14] L. van der Elst, C. Faccini de Lima, M. Gokce Kurtoglu, V.N. Koraganji, M. Zheng, A. Gumennik, 3D printing in fiber-device technology, Adv. Fiber Mater. 3 (2) (2021) 59–75, https://doi.org/10.1007/s42765-020-00056-6.
[15] F. Leng, M. Zheng, C. Xu, 3D-printed microneedles with open groove channels for liquid extraction, Explorations 1 (3) (2021), https://doi.org/10.1002/exp.20210109.
[16] Q. Gu, E. Tomaskovic-Crook, R. Lozano, Y. Chen, R.M. Kapsa, Q. Zhou, G. G. Wallace, J.M. Crook, Functional 3D neural mini-tissues from printed gel-based bioink and human neural stem cells, Adv. Healthc. Mater. 5 (12) (2016) 1429–1438, https://doi.org/10.1002/adhm.201600095.
[17] Y. Zhang, H. Chen, X. Long, T. Xu, Three-dimensional-engineered bioprinted in vitro human neural stem cell self-assembling culture model constructs of Alzheimer's disease, Bioact. Mater. 11 (2022) 192–205, https://doi.org/10.1016/j.bioactmat.2021.09.023.
[18] J. Kapr, L. Petersilie, T. Distler, I. Lauria, F. Bendt, C.M. Sauter, A.R. Boccaccini, C. R. Rose, E. Fritsche, Human induced pluripotent stem cell-derived neural progenitor cells produce distinct neural 3D in vitro models depending on alginate/gellan gum/laminin hydrogel blend properties, Adv. Healthc. Mater. 10 (16) (2021), e2100131, https://doi.org/10.1002/adhm.202100131.
[19] D. Joung, V. Truong, C.C. Neitzke, S.Z. Guo, P.J. Walsh, J.R. Monat, F. Meng, S. H. Park, J.R. Dutton, A.M. Parr, M.C. McAlpine, 3D printed stem-cell derived neural progenitors generate spinal cord scaffolds, Adv. Funct. Mater. 28 (39) (2018), https://doi.org/10.1002/adfm.201801850.
[20] D. Joung, V. Truong, C.C. Neitzke, S.Z. Guo, P.J. Walsh, J.R. Monat, F. Meng, S. H. Park, J.R. Dutton, A.M. Parr, M.C. McAlpine, 3D printed stem-cell derived neural progenitors generate spinal cord scaffolds, Adv. Funct. Mater. 28 (39) (2018), 1801850, https://doi.org/10.1002/adfm.201801850.
[21] X. Liu, M. Hao, Z. Chen, T. Zhang, J. Huang, J. Dai, Z. Zhang, 3D bioprinted neural tissue constructs for spinal cord injury repair, Biomaterials 272 (2021), 120771, https://doi.org/10.1016/j.biomaterials.2021.120771.
[22] C. Gao, Y. Li, X. Liu, J. Huang, Z. Zhang, 3D bioprinted conductive spinal cord biomimetic scaffolds for promoting neuronal differentiation of neural stem cells and repairing of spinal cord injury, Chem. Eng. J. (2022), 138788.
[23] X. Liu, S. Song, Z. Chen, C. Gao, Y. Li, Y. Luo, J. Huang, Z. Zhang, Release of O-GlcNAc transferase inhibitor promotes neuronal differentiation of neural stem cells in 3D bioprinted supramolecular hydrogel scaffold for spinal cord injury repair, Acta Biomater. (2022), https://doi.org/10.1016/j.actbio.2022.08.031.
[24] L. Li, R. Hao, J. Qin, J. Song, X. Chen, F. Rao, J. Zhai, Y. Zhao, L. Zhang, J. Xue, Electrospun fibers control drug delivery for tissue regeneration and cancer therapy, Adv. Fiber Mater. 4 (6) (2022) 1375–1413, https://doi.org/10.1007/s42765-022-00198-9.
[25] J.W. Nichol, S.T. Koshy, H. Bae, C.M. Hwang, S. Yamanlar, A. Khademhosseini, Cell-laden microengineered gelatin methacrylate hydrogels, Biomaterials 31 (21) (2010) 5536–5544, https://doi.org/10.1016/j.biomaterials.2010.03.064.
[26] R.Z. Lin, Y.C. Chen, R. Moreno-Luna, A. Khademhosseini, J.M. Melero-Martin, Transdermal regulation of vascular network bioengineering using a photopolymerizable methacrylated gelatin hydrogel, Biomaterials 34 (28) (2013) 6785–6796, https://doi.org/10.1016/j.biomaterials.2013.05.060.
[27] J.A. Burdick, C. Chung, X. Jia, M.A. Randolph, R. Langer, Controlled degradation and mechanical behavior of photopolymerized hyaluronic acid networks, Biomacromolecules 6 (1) (2005) 386–391, https://doi.org/10.1021/bm049508a.
[28] K.K. Johe, T.G. Hazel, T. Muller, M.M. Dugich-Djordjevic, R.D. McKay, Single factors direct the differentiation of stem cells from the fetal and adult central nervous system, Genes Dev. 10 (24) (1996) 3129–3140, https://doi.org/10.1101/gad.10.24.3129.
[29] M.A. Anderson, T.M. O'Shea, J.E. Burda, Y. Ao, S.L. Barlatey, A.M. Bernstein, J. H. Kim, N.D. James, A. Rogers, B. Kato, A.L. Wollenberg, R. Kawaguchi, G. Coppola, C. Wang, T.J. Deming, Z. He, G. Courtine, M.V. Sofroniew, Required growth facilitators propel axon regeneration across complete spinal cord injury, Nature 561 (7723) (2018) 396–400, https://doi.org/10.1038/s41586-018-0467-6.
[30] D.M. Basso, M.S. Beattie, J.C. Bresnahan, A sensitive and reliable locomotor rating scale for open field testing in rats, J. Neurotrauma 12 (1) (1995) 1–21, https://doi.org/10.1089/neu.1995.12.1.
[31] A. Ramón-Cueto, M.I. Cordero, F.F. Santos-Benito, J. Avila, Functional recovery of paraplegic rats and motor axon regeneration in their spinal cords by olfactory ensheathing glia, Neuron 25 (2) (2000) 425–435, https://doi.org/10.1016/s0896-6273(00)80905-8.
[32] W. Man, S. Yang, Z. Cao, J. Lu, X. Kong, X. Sun, L. Zhao, Y. Guo, S. Yao, G. Wang, X. Wang, A multi-modal delivery strategy for spinal cord regeneration using a composite hydrogel presenting biophysical and biochemical cues synergistically, Biomaterials 276 (2021), 120971, https://doi.org/10.1016/j.biomaterials.2021.120971.
[33] T. Yuan, Y. Shao, X. Zhou, Q. Liu, Z. Zhu, B. Zhou, Y. Dong, N. Stephanopoulos, S. Gui, H. Yan, D. Liu, Highly Permeable DNA Supramolecular Hydrogel Promotes Neurogenesis and Functional Recovery after Completely Transected Spinal Cord Injury, Advanced Materials, Deerfield Beach, Fla., 2021, e2102428, https://doi.org/10.1002/adma.202102428.
[34] Z.-y. Yang, Y.-y. Zhong, J. Zheng, Y. Liu, T. Li, E. Hu, X.-f. Zhu, R.-q. Ding, Y. Wu, Y. Zhang, T. Tang, F. He, S.-s. Wang, Y. Wang, Fmoc-amino acid-based hydrogel vehicle for delivery of amygdalin to perform neuroprotection, Smart Mater. Med. 2 (2021) 56–64, https://doi.org/10.1016/j.smaim.2020.10.004.
[35] M.A. Wozniak, C.S. Chen, Mechanotransduction in development: a growing role for contractility, Nat. Rev. Mol. Cell Biol. 10 (1) (2009) 34–43.
[36] S.K. Seidlits, Z.Z. Khaing, R.R. Petersen, J.D. Nickels, J.E. Vanscoy, J.B. Shear, C. E. Schmidt, The effects of hyaluronic acid hydrogels with tunable mechanical properties on neural progenitor cell differentiation, Biomaterials 31 (14) (2010) 3930–3940.
[37] J.M. Unagolla, A.C. Jayasuriya, Hydrogel-based 3D bioprinting: a comprehensive review on cell-laden hydrogels, bioink formulations, and future perspectives, Appl. Mater. Today 18 (2020), 100479, https://doi.org/10.1016/j.apmt.2019.100479.
[38] B.N. Kharbikar, P. Mohindra, T.A. Desai, Biomaterials to enhance stem cell transplantation, Cell Stem Cell 29 (5) (2022) 692–721, https://doi.org/10.1016/j.stem.2022.04.002.
[39] M.B. Orr, J.C. Gensel, Spinal cord injury scarring and inflammation: therapies targeting glial and inflammatory responses, Neurotherapeutics 15 (3) (2018) 541–553, https://doi.org/10.1007/s13311-018-0631-6.
[40] J.C. Gensel, B. Zhang, Macrophage activation and its role in repair and pathology after spinal cord injury, Brain Res. 1619 (2015) 1–11, https://doi.org/10.1016/j.brainres.2014.12.045.
[41] J.Y. Mao, L. Chen, Z.W. Cai, S.T. Qian, Z.M. Liu, B.F. Zhao, Y.G. Zhang, X.M. Sun, W.G. Cui, Advanced biomaterials for regulating polarization of macrophages in wound healing, Adv. Funct. Mater. 32 (12) (2022), 2111003, https://doi.org/10.1002/adfm.202111003.
[42] Z. Gong, D. Lei, C. Wang, C. Yu, K. Xia, J. Shu, L. Ying, J. Du, J. Wang, X. Huang, L. Ni, C. Wang, J. Lin, F. Li, Z. You, C. Liang, Bioactive elastic scaffolds loaded with neural stem cells promote rapid spinal cord regeneration, ACS Biomater. Sci. Eng. 6 (11) (2020) 6331–6343, https://doi.org/10.1021/acsbiomaterials.0c01057.
[43] T. Tylek, C. Blum, A. Hrynevich, K. Schlegelmilch, T. Schilling, P.D. Dalton, J. Groll, Precisely defined fiber scaffolds with 40 mum porosity induce elongation driven M2-like polarization of human macrophages, Biofabrication 12 (2) (2020), 025007, https://doi.org/10.1088/1758-5090/ab5f4e.
[44] J. Qian, Z. Lin, Y. Liu, Z. Wang, Y. Lin, C. Gong, R. Ruan, J. Zhang, H. Yang, Functionalization strategies of electrospun nanofibrous scaffolds for nerve tissue engineering, Smart Mater. Med. 2 (2021) 260–279, https://doi.org/10.1016/j.smaim.2021.07.006.
[45] L. Yan, K. Han, B. Pang, H. Jin, X. Zhao, X. Xu, C. Jiang, N. Cui, T. Lu, J. Shi, Surfactin-reinforced gelatin methacrylate hydrogel accelerates diabetic wound healing by regulating the macrophage polarization and promoting angiogenesis, Chem. Eng. J. 414 (2021), 128836, https://doi.org/10.1016/j.cej.2021.128836.
[46] S. Hauck, P. Zager, N. Halfter, E. Wandel, M. Torregrossa, A. Kakpenova, S. Rother, M. Ordieres, S. Rathel, A. Berg, S. Moller, M. Schnabelrauch, J.C. Simon, V. Hintze, S. Franz, Collagen/hyaluronan based hydrogels releasing sulfated hyaluronan improve dermal wound healing in diabetic mice via reducing inflammatory macrophage activity, Bioact. Mater. 6 (12) (2021) 4342–4359, https://doi.org/10.1016/j.bioactmat.2021.04.026.
[47] Z. Cheng, W. Zhu, K. Cao, F. Wu, J. Li, G. Wang, H. Li, M. Lu, Y. Ren, X. He, Anti-inflammatory mechanism of neural stem cell transplantation in spinal cord injury, Int. J. Mol. Sci. 17 (9) (2016) 1380, https://doi.org/10.3390/ijms17091380.
[48] Y. Gao, X. Chen, T. Tian, T. Zhang, S. Gao, X. Zhang, Y. Yao, Y. Lin, X. Cai, A lysosome-activated tetrahedral nanobox for encapsulated siRNA delivery, Adv. Mater. 34 (46) (2022), e2201731, https://doi.org/10.1002/adma.202201731.
[49] J. Li, Y. Yao, Y. Wang, J. Xu, D. Zhao, M. Liu, S. Shi, Y. Lin, Modulation of the crosstalk between Schwann cells and macrophages for nerve regeneration: a therapeutic strategy based on a multifunctional tetrahedral framework nucleic acids system, Adv. Mater. 34 (46) (2022), e2202513, https://doi.org/10.1002/adma.202202513.
[50] I.B. Wanner, M.A. Anderson, B. Song, J. Levine, A. Fernandez, Z. Gray-Thompson, Y. Ao, M.V. Sofroniew, Glial scar borders are formed by newly proliferated, elongated astrocytes that interact to corral inflammatory and fibrotic cells via STAT3-dependent mechanisms after spinal cord injury, J. Neurosci. 33 (31) (2013) 12870–12886, https://doi.org/10.1523/JNEUROSCI.2121-13.2013.
[51] J. Zhu, Y. Yang, W. Ma, Y. Wang, L. Chen, H. Xiong, C. Yin, Z. He, W. Fu, R. Xu, Y. Lin, Antiepilepticus effects of tetrahedral framework nucleic acid via inhibition of gliosis-induced downregulation of glutamine synthetase and increased AMPAR internalization in the postsynaptic membrane, Nano Lett. 22 (6) (2022) 2381–2390, https://doi.org/10.1021/acs.nanolett.2c00025.
[52] A.P. Tran, P.M. Warren, J. Silver, The biology of regeneration failure and success after spinal cord injury, Physiol. Rev. 98 (2) (2018) 881–917, https://doi.org/10.1152/physrev.00017.2017.
[53] L. Xia, J. Qi, M. Tang, J. Liu, D. Zhang, Y. Zhu, B. Hu, Continual deletion of spinal microglia reforms astrocyte scar favoring axonal regeneration, Front. Pharmacol. 13 (2022), 881195, https://doi.org/10.3389/fphar.2022.881195.
[54] E.J. Bradbury, E.R. Burnside, Moving beyond the glial scar for spinal cord repair, Nat. Commun. 10 (1) (2019) 3879, https://doi.org/10.1038/s41467-019-11707-7.
[55] J.R.d. Cruz Vieira, B. Shah, C. Ruiz de Almodóvar, Cellular and Molecular Mechanisms of Spinal Cord Vascularization, 2020.
[56] Y. Manavski, R.A. Boon, S. Dimmeler, Vascular niche controls organ regeneration, Circ. Res. 114 (7) (2014) 1077–1079, https://doi.org/10.1161/CIRCRESAHA.114.303452.
[57] D. Chung, A. Shum, G. Caraveo, GAP-43 and BASP1 in axon regeneration: implications for the treatment of neurodegenerative diseases, Front. Cell Dev. Biol. 8 (2020), 567537, https://doi.org/10.3389/fcell.2020.567537.
[58] F.D. Miller, A. Gauthier-Fisher, Home at last: neural stem cell niches defined, Cell Stem Cell 4 (6) (2009) 507–510.
[59] H.K. Lee, L.S. Chaboub, W. Zhu, D. Zollinger, M.N. Rasband, S.P. Fancy, B. Deneen, Daam2-PIP5K is a regulatory pathway for Wnt signaling and therapeutic target for

remyelination in the CNS, Neuron 85 (6) (2015) 1227–1243, https://doi.org/10.1016/j.neuron.2015.02.024.

[60] B.Q. Lai, X. Zeng, W.T. Han, M.T. Che, Y. Ding, G. Li, Y.S. Zeng, Stem cell-derived neuronal relay strategies and functional electrical stimulation for treatment of spinal cord injury, Biomaterials 279 (2021), 121211, https://doi.org/10.1016/j.biomaterials.2021.121211.

[61] L. Li, B. Xiao, J. Mu, Y. Zhang, C. Zhang, H. Cao, R. Chen, H.K. Patra, B. Yang, S. Feng, Y. Tabata, N.K.H. Slater, J. Tang, Y. Shen, J. Gao, A MnO2 nanoparticle-dotted hydrogel promotes spinal cord repair via regulating reactive oxygen species microenvironment and synergizing with mesenchymal stem cells, ACS Nano 13 (12) (2019) 14283–14293, https://doi.org/10.1021/acsnano.9b07598.